Functionally graded scaffold with M2 macrophage-derived LncRNA-Encoded peptide: Mechanistic and therapeutic evaluation for rotator cuff repair

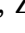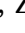Hao Feng [a,1], Gonghao Zhang [b,1], Li Xiong [b,1], Panpan Shang [c], Xiao Yu [a], Bin Chai [b], Lu Han [a], Shuqi Lou [a], Muhammad Shafiq [d], Yiying Zhang [e], Mohamed EL-Newehy [f], Meera Moydeen Abdulhameed [f], Zhengchao Yuan [a,*], Xiumei Mo [a,c,**], Yunhan Ji [b,***]

a State Key Laboratory for Modification of Chemical Fibers and Polymer Materials, Shanghai Engineering Research Center of Nano-Biomaterials and Regenerative Medicine, College of Biological Science and Medical Engineering, Donghua University, Shanghai, 201620, China
b Department of Orthopedics, Tongren Hospital Shanghai Jiao Tong University School of Medicine, Shanghai, 200336, China
c Institute of Biomaterials and Biomedicine, School of Food and Pharmacy, Shanghai Zhongqiao Vocational and Technical University, Shanghai, 201514, China
d Innovation Center of NanoMedicine (iCONM), Kawasaki Institute of Industrial Promotion, Kawasaki-ku, Kawasaki, 210-0821, Japan
e School of Chemistry and Chemical Engineering, Southeast University, Nanjing, 211189, China
f Department of Chemistry, College of Science, King Saud University, P.O. Box 2455, Riyadh 11451, Saudi Arabia

ARTICLE INFO

ABSTRACT

The rotator cuff is prone to tear under degenerative changes or mechanical injury, leading to excessive inflammation, extracellular matrix degradation, and unsatisfactory prognosis. Interleukin-4 (IL-4) was used to induce macrophages polarization toward M2 phenotype. By mapping IL 4-activated pathways and applying peptidome profiling, macrophage-derived peptide 1 (MDP1) was identified and shown to promote the phosphorylation of STAT3 and STAT6, thereby inducing the polarization of M0 macrophages toward the anti-inflammatory M2 phenotype. A functionally graded scaffold woven from electrospun nanofiber yarns was developed, with MDP1 and hydroxyapatite (HA) loaded onto its corresponding interfaces. During rotator cuff repair process, the scaffold functioned as an augmentation patch, with mechanical properties (Young's modulus, ca. 280 MPa) comparable to native tendons, prevented rotator cuff re-tearing in an early stage. MDP1 was incorporated into scaffolds to modulate an excessive inflammatory response, while HA was used to enhance biomineralization for enhanced osteointegration. Through a multidimensional collaborative repair strategy, this functionally graded scaffold not only mimicked the tendon–bone interface, but also significantly suppressed local inflammation at the interface, as evidenced by a 60.6 % and 66.5 % reduction in IL-6–positive areas at 2 and 4 months, respectively, compared with the control group. Furthermore, it promoted tissue regeneration in the damaged region, resulting in a 32.6 % increase in Young's modulus, thereby ultimately enhancing rotator cuff performance. The multifunctionally graded scaffold may offer an invaluable solution to promote rotator cuff tear healing and potentially other related disciplines.

1. Introduction

Rotator cuff injuries are a prevalent clinical musculoskeletal disorder that typically present as a spectrum of pathologies ranging from tendon degeneration to partial tears, progressing to complete tears, and ultimately evolving into rotator cuff tear arthropathy [1]. Rotator cuff tears

---

are often accompanied by varying degrees of pain and can affect shoulder mobility. Annually, more than 4 million new tendon-bone injury cases are reported worldwide, with rotator cuff and the anterior cruciate ligament (ACL) being the most frequently affected [2]. The incidence of rotator cuff tears increases significantly in the aging population, with over 50 % of individuals aged 65 and above presenting with such injuries [3].

For patients with mild rotator cuff tears (<1 cm), early-stage conservative treatment strategies, including physical therapy, bracing, and corticosteroid injections are widely implemented to alleviate symptoms, although numerous studies indicated that long-term use of corticosteroid injection does not result in significant functional improvement in rotator cuff repair [4,5]. When conservative measures are proved to be ineffective, full-thickness rotator cuff repair becomes the preferred intervention. For patients with severe tears, surgical interventions, such as arthroscopic techniques are widely adopted [6]. Nonetheless, current surgical practices primarily focus on the reattachment of the remaining tendon to the footprint region, thereby neglecting the critical tendon-bone interface responsible for an efficient stress transfer [2]. This repair paradigm frequently results in suboptimal outcomes, with postoperative retear rates ranging from 13 % to 94 %, highlighting the limitations of current therapeutic strategies [7].

The complexity of the tendon-bone interface is one of the principal factors contributing to the high failure rates of surgical repairs [3,8–10]. This interface is structurally composed of highly heterogeneous tissues, which can be divided into four distinct regions based on the direction of mechanical load, including tendon, non-mineralized fibrocartilage, mineralized fibrocartilage, and bone. The tendon region is mainly composed of highly organized type I collagen (COL I) fibers, which self-assembles in a hierarchical manner, ranging from the nanoscale to the microscale [11–14]. Both non-mineralized and mineralized fibrocartilage are mainly composed of collagen type II (COL II) and collagen type III (COL III); the mineralized fibrocartilage is reinforced with nanometer-scale mineral deposits. Bone tissues are comprised of mineralized COL I fibers [15]. This transitional zone plays a crucial role in eliminating stress concentration, without this transition, the mismatch in mechanical properties between the tendon (low modulus) and bone (high modulus) induces stress concentrations, thereby contributing to further tissue damage and failure [16,17]. Unfortunately, current surgeries are unable to reconstruct the functionally graded transition at the tendon-bone interface.

Sustained inflammatory response during healing process is another significant contributor to the poor rotator cuff healing after surgery [18]. In early stages of rotator cuff injury, immune cells are rapidly recruited to the injury site, with pro-inflammatory cytokine expression peaking several fold within the first three days of the injury [19]. On the other hand, in later healing stages, the loss of anti-inflammatory (M2) macrophages occurs, which are essential for balancing inflammation, thereby suppressing fibrocartilage regeneration. This region is instead replaced by scar tissue rich in COL III and can significantly compromise the mechanical properties of transition zone. Concurrently, inflammatory microenvironment triggers a cascade of immune responses, resulting in cell apoptosis, extracellular matrix (ECM) degradation, and tissue fibrosis [20]. Therefore, regulating the proportion of M2 macrophages during tendon-bone healing may be pivotal to suppress excessive inflammation and promote an effective repair at the tendon-bone interface.

Macrophages-derived peptide 1 (MDP1) is a small bioactive peptide (MCSVLLGIGLLEFGLLNTRLIKSQSFIRMRYLRGRGGR) selected from a library of 231 peptides derived from M2 macrophages, which exhibits optimal biological activity, favorable aliphatic amino acid index, and high stability. Bioinformatics analysis using the ORFfinder database revealed that MDP1 is derived from the long non-coding RNA MM2P (lncRNA MM2P), which indicates that the MDP1 may share regulatory functions with lncRNA MM2P in modulating M2 macrophages polarization. LncRNA MM2P has been identified as the only lncRNA that is specifically upregulated during M2 macrophages polarization and downregulated during M1 macrophages polarization [21]. An over-expression of lncRNA MM2P can activate Signal Transducer and Activator of Transcription 3 (STAT3) signaling by inhibiting SH2 domain-containing protein tyrosine phosphatase 2 (SHP2)-mediated dephosphorylation of STAT3, whereas silencing SHP2 suppresses the increased proportion of M1 macrophages [22].

Similarly, lncRNA MM2P may indirectly regulate the dephosphorylation of STAT6, thereby modulating M2 gene expression [21]. Therefore, it is a reasonable to hypothesize that MDP1 may regulate M2 macrophages polarization through a pathway similar to that of lncRNA MM2P. Bai et al. found that the increased levels of p-STAT3 enhanced the gene expression of SOX9, a cartilage repair modulator, which may promote cartilage formation by regulating the expression of collagen type II alpha 1 COL2A1 and aggrecan [23]. LaBranche et al. reported STAT3-mediated reduction in bone resorption in an inflammatory arthritis animal model, which was driven by the reduced receptor activator of nuclear factor kappa-B (RANKL) levels as well as diminished activity of osteoclasts [24]. Therefore, the regulation of STAT3 and STAT6 levels by lncRNA MM2P may influence tendon, fibrocartilage, and bone regeneration through multiple pathways. MDP1 can promote the healing of tendon-bone interface by regulating excessive inflammation and modulating growth factor levels through similar pathways.

Hydroxyapatite (HA) is widely used as a bone substitute, thanks to its similarity to the inorganic components of bone tissue as well as its excellent biocompatibility. HA particles have also been proven to enhance osteogenic differentiation of stem cells as well as improve the mechanical properties and bioactivity of bone scaffolds, which may be pivotal to promote tendon-bone healing as well as reinforce an overall structural integrity of the tendon-bone interface [25].

Electrospinning is widely used to fabricate tissue-engineered scaffolds. Electrospun fibers can recapitulate ECM's morphology and they may additionally help incorporate different types of bioactive cues to modulate tissue repair process [26]. Electrospinning can be broadly categorized into four types: traditional electrospinning, co-axial electrospinning, emulsion electrospinning, and dynamic flow electrospinning [27]. As a special form of traditional electrospinning, double-spray electrospinning is often employed to match the mechanical properties of the scaffold with the tendon-bone interface as closely as possible. Briefly, two nozzles with opposite charges eject the prepared electrospinning solution. The fibers with opposite charges intertwine and are evenly deposited onto a silk fibroin yarn (SF yarn, which serves as a reinforcing core). The fiber-coated yarn is further assembled onto a collector for the subsequent use. The yarn exhibits excellent mechanical properties and uniform drug loading.

In recent years, the concept of patch augmentation has emerged as a promising auxiliary strategy to improve clinical outcomes in arthroscopic rotator cuff repair. This approach utilizes biological or synthetic materials to reinforce native tendon repairs, promote tissue regeneration, and enhance biomechanical stability. Compared with traditional repair techniques, patch augmentation holds potential to reduce the risk of re-tear, provide structural support at the repair site, and improve the integrity and durability of healing tissue [28].

Therefore, a functionally graded scaffold was developed in this study as a biofunctional augmentation patch that mimics the native tendon–bone interface while actively promoting tissue regeneration. Firstly potential structures of different types of peptides derived from lncRNA MM2P were predicted using AlphaFold3, and relevant biochemical coefficients were calculated (Information of peptides is provided in Table S1). Among all of these, MDP1, which exhibited the best stability and activity was selected and synthesized via Fmoc solid-phase synthesis. Afterwards, three groups of spinning solutions were prepared with the following compositions: Group A composed of poly(L-lactide-co-ε-caprolactone) (PLCL) and silk fibroin (SF, a protein with good biocompatibility and mechanical properties [29]); Group B composed of PLCL, SF and MDP1; and Group C composed of PLCL, SF and HA
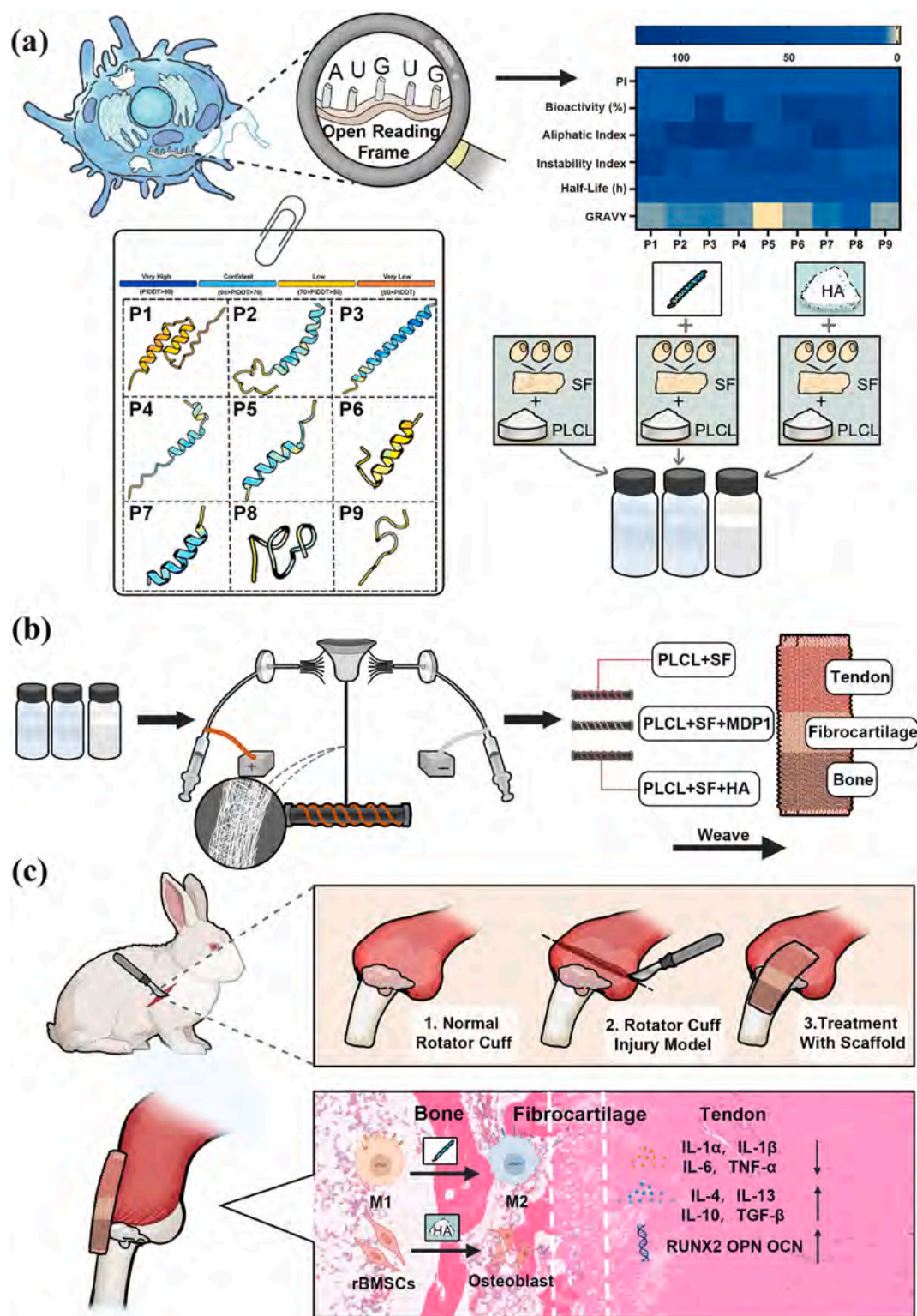
Fig. 1. Systematic illustration of the preparation and implantation of the MDP1&HA-loaded scaffold. (a) Structural prediction and biochemical coefficient of the peptide derived from lncRNA MM2P. (b) Preparation of corresponding nanofiber yarns from different electrospinning solutions, followed by woven into scaffolds. (c) Establishment of rotator cuff tear model and regulation of tendon-bone interface at cellular level by MDP1 and HA.

(Fig. 1a). Group A, B, and C were used to simulate tendon interface, fibrocartilage interface, and bone tissue, respectively. These three spinning solutions were electrospun into nanofiber on SF yarn. These three types of nanofiber yarns were collected and woven into a functionally graded scaffold to simulate the transitional structure of the tendon-bone interface (Fig. 1b). A full-thickness rotator cuff tear model was established using New Zealand rabbits through surgical cutting of the rotator cuff. After implantation *in vivo*, MDP1 and HA could exert their respective functions at the cellular level (Fig. 1c).

2. Experimental section

2.1. Materials

PLCL (LA:CL = 75:25, IV = 2.8 dl/g) was purchased from Shenzhen Match Biomaterials Co., Ltd. (Shenzhen, China). SF was extracted from silkworm cocoons (Northwest Sericulture Base, Shaanxi, China). Sodium carbonate (Na_2CO_3) and lithium bromide (LiBr) were purchased from Rhawn Co., Ltd. (Shanghai, China). MDP1 and RgM were synthesized by QYAOBIO (ChinaPeptides Co., Ltd.). HA was purchased from Anhui Senrise Technology Co., Ltd. (Anhui, China). SF yarn was obtained from Huguang Development Co., Ltd. (Shanghai, China). 1,1,1,3,3,3-Hexa-fluoro-2-propanol (HFIP) was purchased from Shanghai Jiu Ming Trading Co., Ltd. (Shanghai, China). CD86 (catalogue # 105005, 50 μg) and CD206 (catalogue # 141705, 25 μg) were purchased from Bio-Legend, Inc. (California, USA). The following kits were obtained from Beyotime Biotechnology Co., Ltd. (Chengdu, China): Endotoxin detection kit (catalogue #C0276S), NO detection kit (catalogue #S0021S), ROS detection kit (catalogue #S0033S), CCK-8 kit (catalogue # 0042), Calcein/PI cell viability/cytotoxicity assay kit (catalogue #C2015M), Alcian blue staining kit (catalogue #C621S), Safranine O staining kit (catalogue #C0155S), Alizarin Red S staining kit (catalogue # 1038), Alkaline phosphatase staining kit for pluripotent stem cells (catalogue #C3250S), Alkaline Phosphatase assay kit (catalogue #P0321S), BCA protein assay kit (catalogue #P0010S). SD rats were purchased from Shanghai JieSiJie Laboratory Animal Co., Ltd. (Shanghai, China). RAW264.7 macrophages and L929 fibroblasts were obtained from the Cell Bank of the Chinese Academy of Sciences (Shanghai, China).

2.2. Preparation of nanofiber yarns and scaffolds

2.2.1. Characterization of peptides

High-performance liquid chromatography (HPLC) was performed to discern the purity of the synthesized peptide and electrospray ionization mass spectrometry (ESI-MS) was employed to determine the molecular weight of the synthesized peptide. The endotoxin level of the peptide was also assessed to determine whether the synthesized peptide was suitable for use in cell-based immunological experiments. The detailed methods are provided in Supplementary Information, and the results are listed in Supplementary Fig. S1.

2.2.2. Extraction of silk fibroin

Silk fibroin (SF) was prepared according to an established protocol [30]. Briefly, sodium carbonate (Na_2CO_3) was dissolved in 6 L of boiling deionized (DI) water to obtain a 0.6 mol/L solution. Silk cocoons (60 g) were cut into 2×2 cm^2 fragments, immersed into Na_2CO_3 solution, and boiled at 100 °C for 30 min. After each boiling step, silk cocoons were manually shredded to facilitate the removal of sericin and other impurities. This process was repeated two times to ensure the complete purification. The resulting material was then washed with DI water and dried in an oven at 100 °C for 24 h. 10 g of degummed SF was added to a 9.1 mol/L LiBr solution and the mixture was stirred until complete dissolution, and filtered. The resulting solution was dialyzed using a dialysis membrane with a Molecular Weight Cut-Off (MWCO) of 14 kDa for at least 72 h to remove excess LiBr. The purified silk fibroin was lyophilized and stored at −20 °C until use. The products from each step during the extraction process are shown in Supplementary Fig. S2.

2.2.3. Electrospining of nanofiber yarns

Three types of electrospinning solutions were prepared for tendon interface, fibrocartilage interface, and bone interface, namely, Group A, Group B, and Group C, respectively. Group A was composed of 0.75 g of PLCL and 0.25 g of SF. Group B was composed of 0.75 g of PLCL, 0.25 g of SF, and different content of MDP1 in the range of 0.05 mg–5 mg; while Group C included 0.75 g PLCL, 0.25 g SF, and 0.1g HA. Each formulation was dissolved in 10 mL HFIP under continuous magnetic stirring at room temperature (r.t.) for 12 h to ensure homogeneous mixing. Once completely dissolved, the solutions were electrospun uniformly onto the surface of SF yarns using a double-spray electrospinning (TEADFS-700, BJTECHNOVA, Beijing, China), with positive and negative high-voltage charges applied to fabricate nanofiber for each interface type. Electrospinning parameters were optimized as follows: applied voltage, 8.5 kV, flow rate of solution, 0.03 mL/min, winding roll speed 400 rotations per minute (rpm), the distance between the winding roll and the two spinnerets, 15 cm and a rotation speed of collector, 10 rpm. The ambient relative humidity was controlled at 30 %–40 % and the electrospinning process was carried out at r.t.

Nanofiber yarns were named according to their composition. Yarns composed of Group A were named as PS, those from the Group B with 0.005 mg/mL, 0.01 mg/mL, 0.05 mg/mL, 0.125 mg/mL, 0.25 mg/mL, and 0.5 mg/mL of MDP1 were named as PS-M1, PS-M2, PS-M3, PS-M4, PS-M5 and PS-M6 separately. On the other hand, yarns electrospun from Group C were named as PS-HA.

2.2.4. Weaving of scaffolds

The SF yarns coated with different types of nanofibers were labeled as PS, PS-M, and PS-HA respectively. For scaffold fabrication, three distinct types of tissue-mimicking constructs were developed using a fully automated multi-shuttle branching pipeline weaving machine (YASL2300-12-24, Yaselin, China). All scaffolds used PS yarns as warp threads along with nanofiber comprised of different combination of biomaterials to achieve tissue-specific characteristics: the tendon-mimicking scaffold (4.94 mm × 4.22 mm) used PS weft threads, the fibrocartilage-mimicking scaffold (5.31 mm × 4.94 mm) incorporated PS-M weft yarns, and the bone-mimicking scaffold (5.56 mm × 4.94 mm) employed PS-HA weft threads.

2.3. Characterization of nanofiber yarns and scaffolds

Scanning electron microscopy (SEM, Hitachi, TM-1000, Tokyo, Japan) was used to observe the surface morphology of the yarns. PS, PS-M and PS-HA was prepared separately and gold-sputtered for 60 s prior to morphological analysis. The morphology of nanofiber yarns was observed at different magnifications. Fiji (ImageJ, version 1.54g) was used to ascertain the distribution of diameter of fibers deposited on the yarn surface.

PS, PS-M, PS-HA, and SF yarns were weighed and subjected to thermogravimetric analysis (TGA, SQ8-STA800, CLARUS, Netherland). Thermal stability was assessed in the temperature range of 25 °C–800 °C at a heating rate of 10 °C/min. For degradation *in vitro*, PS, PS-M, and PS-HA scaffolds were sterilized, accurately weighed, and then immersed in phosphate buffer solution (PBS) at 37 °C for up to different time points. At 1, 2, 4, 8, and 12 weeks, the scaffolds were removed from the PBS, freeze-dried, and weighed.

Since the release of MDP1 cannot be directly detected, RgM was used as a substitute to delineate the release kinetics of MDP1. The calibration curve of the RgM was prepared using the known concentrations of RgM. Approximately 20 mg of sterilized PS-RgM scaffolds were incubated with 20 mL PBS under shaking conditions (60 rpm) at 37 °C. The release medium was collected at day 1, 3, 5, 7 as well as at week 2, 3, 4 and the absorbance of the solution was measured at 550 nm. The cumulative release was ascertained using RgM standard curve.

On the other hand, the cumulative release of HA was assessed with Inductively Coupled Plasma (ICP, EXPEC7350, EXPEC, China). Approximately 20 mg of sterilized PS-HA scaffolds were incubated with 20 mL PBS under shaking conditions (60 rpm) at 37 °C. Supernatants were collected on day 1, 3, 5, 7, and week 2, 3, 4, filtered through a 0.22 μm filter, and analyzed. The concentration of calcium ion (Ca^{2+}) was determined by comparing with the standard curve.

The structural analysis was carried out with Fourier Transform Infrared Spectroscopy (FTIR, NEXUS-670, NIEGO, USA). PLCL, SF, HA, and three types of scaffolds were cut into small pieces, and their

absorption spectra were recorded from 4000 cm^{-1} to 500 cm^{-1}.

To delineate if the HA was successfully incorporated into scaffolds, elemental composition of carbon (C), nitrogen (N), oxygen (O), and phosphorus (P) was examined with Field-Emission Scanning Electron Microscopy (FE-SEM, SU8600, Hitachi, Japan). Elemental mapping images were obtained to visualize the distribution of these elements.

Biocompatibility is positively correlated with the hydrophilicity of biomaterial surfaces. Hydrophilic surfaces provide more active sites for cells, facilitating cell adhesion and proliferation. Therefore, the water contact angle (WCA) of PS, PS-M, and PS-HA scaffolds was measured with contact angle goniometer (OCA40, Dataphysics, Germany). A water droplet (ca. 3 μL) was precisely placed on the surface of the sample, and the angle at which the droplet was adhered to the material surface was analyzed with Fiji.

Mechanical properties of yarns and woven scaffolds were evaluated using Instron tensile testing machine (3345, Instron, USA). Briefly, the diameter and original length of nanofiber yarns, as well as the thickness of scaffolds were measured and each sample was fixed in a fixture and subjected to uniaxial stretching at a scan rate of 20 mm/min until the sample was ruptured. Mechanical properties of scaffolds, such as ultimate tensile stress (UTS), Young's modulus (*E*), and strain at failure were measured using representative stress-strain curves.

2.4. Anti-inflammatory and anti-oxidative properties

Flow cytometry was used to discern the phenotypes of macrophages. RAW264.7 macrophages (1×10^6) were seeded in a 6-well plate and cultured with the medium containing 0.5 mg/mL of LPS, extract solution of scaffolds with different concentrations of MDP1, ranging from PS (control) to PS-M6, and 0.5 mg/mL of LPS along with PS-M4 for up to 12 h. Cells were collected by centrifugation at 1300 rpm for 3 min and incubated with CD86 antibody (diluted 100 × in PBS) at 37 °C for 30 min. Cells were then washed with 1.5 mL PBS, centrifuged, and resuspended in 0.5 mL of 2 % BSA for blocking for 30 min. Finally, cells were incubated with CD206 antibody (diluted with PBS, 1:80, v/v) at 37 °C for 30 min. After PBS washing to remove unbound CD206, cells were collected by centrifugation, resuspended in 200 μL PBS, filtered through a mesh, and analyzed by flow cytometer (Attune NxT, Thermo Fisher Scientific, USA). In addition, single-stained tubes for CD86 and CD206 antibodies were used for flow cytometry compensation, and data analysis was performed using FlowJo.

Anti-oxidative properties of MDP1-loaded scaffolds were ascertained with NO clearance assay and ROS scavenging assay. RAW264.7 macrophages (1×10^6) were seeded in a 6-well plate and cultured with medium containing 0.5 mg/mL LPS or with the extract solution of scaffolds with different concentrations of MDP1, ranging from PS-M4 to PS-M6, for up to 12 h. The supernatant was aspirated and analyzed with the manufacturer's instructions of NO clearance assay kit. The NO clearance (%) was calculated by equation (1):

$$\text{NO Clearance (\%)} = \frac{A_N - A_S}{A_N} \times 100\% \tag{1}$$

Where A_N represents the absorbance of LPS group at 540 nm, while A_S represents the absorbance of PS-M4, PS-M5 and PS-M6 group at 540 nm.

ROS detection kit was used to measure the ROS levels. The DCFH-DA solution was diluted (10 μM) with PBS, and 1 mL of the diluted DCFH-DA solution was added into plates and incubated at 37 °C for 20 min. Subsequently, DAPI solution was added to each well and cells were incubated for an additional 20 min. Cells were washed with PBS and observed using a confocal laser scanning microscope (CLSM, STELLARIS FALCON, Leica, Germany).

2.5. Cytocompatibility and biological functions of scaffolds in vitro

2.5.1. Isolation of cells and biocompatibility assay

rBMSCs, tenocytes and fibrochondrocytes were harvested from two-week-old Sprague Dawley (SD) rats according to the previous reports [31–33]. RAW264.7 macrophages, tenocytes, fibrochondrocytes, rBMSCs, and L929 fibroblasts were used for biocompatibility and biofunction assay. Cells were seeded in 48-well cell culture plates and cultured with the extract solution of different types of scaffolds containing varying content of MDP1 for up to 7 days. At each time point, the original culture medium was removed, and 370 μL of serum-free medium and 30 μL of WST-8 was added into each well. Cells were incubated at 37 °C for 1 h and the absorbance of the supernatant was measured at 450 nm by microplate reader (Multiskan FC, Thermo Fisher Scientific, USA).

The viability of tenocytes cultured along with the extract solution of different types of scaffolds for up to day 5 was measured using Calcein/PI cell viability/cytotoxicity assay kit following manufacturer's instructions. A total 250 μL of Calcein AM/PI working solution was added into each well in a 24-well cell culture plate and samples were incubated at 37 °C for 30 min under light protection. Cell staining was then observed with CLSM.

2.5.2. IF staining of COL I and COL II

IF staining was used to discern the effects of scaffolds loaded with different concentrations of MDP1 on cell morphology and the expression of relevant markers. To collect the conditional medium, RAW 264.7 macrophages were cultured with the extract solution of different types of scaffolds in LPS-containing medium for 12 h and filtered. The tenocytes were cultured along with the conditioned medium for up to 10 days, while fibrochondrocytes were cultured in the conditioned medium for up to 14 days. The conditional medium was replaced every three days. The culture medium was removed, and cells were fixed with 4 % paraformaldehyde (PFA) at r.t. for 30 min, followed by treatment with 0.5 % Triton X-100 for 30 min. To prevent non-specific cell adsorption, cells were treated with 5 % BSA for 2 h. The primary antibody was diluted 500 × with BSA and samples were incubated overnight at 4 °C along with the diluted primary antibody. Cells were washed with PBS, and secondary antibody (diluted 1000 × with PBS) was added for 1 h under light protection. Cells were washed with PBS and stained with a cytoskeletal fluorescence probe for 30 min. Once washed with PBS, cells were stained with DAPI and imaging was performed with CLSM.

2.5.3. Alcian Blue and Safranine O staining

Alcian Blue selectively stains acidic mucopolysaccharides in cartilage, imparting a blue color, while Safranine O interacts with the anionic groups of proteoglycans in cartilage, resulting in red or purple staining. Upon cartilage injury, the release of glycoproteins causes an uneven distribution of matrix components, leading to altered Alcian Blue and Safranine O staining. Therefore, both Alcian Blue and Safranine O staining are employed to assess the growth of fibrochondrocytes [34]. The conditional culture medium was used to culture fibrochondrocytes for 14 days. After removing the culture medium and washing with PBS, cells were fixed with 4 % PFA and stained following manufacturer's instructions. Since small amounts of Safranine O and Alcian Blue are fully soluble in DMSO, after removing excess dye, DMSO was used to dissolve the stained dye. The absorbance of the solution was measured at 600 nm for Alcian Blue and at 510 nm for Safranine O by microplate reader.

2.5.4. Alkaline Phosphatase (ALP) and Alizarin Red S (ARS) assays

To delineate the effect of the scaffold on osteogenic induction of rBMSCs, ALP and ARS assays were performed. Briefly, osteogenic induction components were added to the conditional culture medium to prepare the conditional and osteogenic induction medium. The composition of the osteogenic inducing conditional medium per 100 mL

was as follows: 10 μL of 0.4 mg/mL dexamethasone, 200 μL of 0.17 mg/mL vitamin C, and 1 mL of 0.3 mg/mL β-glycerophosphate. Approximately, 5×10^6 rBMSCs were seeded in a 24-well cell culture plate and cultured for up to 10 days. ALP and ARS assays were performed according to the kit instructions. To quantify the mineralization of rBMSCs, hexadecylpyridinium chloride was used to dissolve the stained wells, and the absorbance was measured at 570 nm by microplate reader.

2.5.5. Transwell migration assay

Transwell migration assay was carried out to discern the ability of the scaffold to recruit rBMSCs. Cells were cultured in serum-free medium for 12 h and then transferred to the small chambers of the Transwell inserts. Scaffolds with different components were soaked in serum-free medium to obtain extract solution. The extract solution was filtered and added into the lower chamber of the Transwell inserts and cell culture was carried out for 12 h. Cells were fixed with 4 % PFA for 20 min and stained with crystal violet. The upper surface of inserts (non-migrated cells) was gently wiped off with a cotton swab. The migration of rBMSCs was recorded by bright-field imaging by an inverted microscope (DMi1, Leica, Germany) at high magnification (40 ×).

2.6. Western blot and qPCR assays

Western Blot assays were used to evaluate the regulatory effect of MDP1 on the transcription factor levels. qPCR was used to analyze the relative expression level of IL-4, TNF-α in RAW264.7 macrophages; COL I, SCX, and TNC in tenocytes; SOX9, AGG, COL II in fibrochondrocytes, and RUNX2, OPN, and OCN in rBMSCs. The detailed methods are provided in Supplementary Information, and the qPCR primer sequence are listed in Supplementary Table S2.

2.7. Animal experiments

2.7.1. Preparation of scaffolds for implantation

The fabrication steps of scaffolds are similar to the methods mentioned above in Chapter 5.2.3: PS yarns were used as wrap threads, whereas PS, PS-M4 and PS-HA yarns were used as weft threads. Functionally graded scaffolds (5 mm × 15 mm) with continuous compositional variation were fabricated using a fully automated multi-shuttle branching pipeline weaving machine. Scaffolds composed only of PS were used as a control group. All scaffolds were sterilized by UV irradiation before implantation.

2.7.2. Establishment of rotator cuff model

To evaluate *in vivo* tendon-bone interface regeneration ability of functionally graded scaffold, a rotator cuff tear model was established using 16-week-old New Zealand White rabbits. All animal experiments were carried out in accordance with the guidelines approved by the Animal Ethics Committee of Shanghai Tongren Hospital (A2024-031-01). A total of 24 male New Zealand White rabbits were randomly divided into three groups (n = 8 for each group): control group (Suture-repaired), PS scaffold group, and MDP1&HA scaffold group. Rabbits were anesthetized by intraperitoneal injection of 50 mg/kg ketamine and 5 mg/kg xylazine and securely positioned on the surgical table. The fur over the rotator cuff region was shaved, with the surrounding skin disinfected. A skin incision was made to expose the rotator cuff, after which the tendon was isolated and transected along the fibrocartilage layer. A degradable 5-0 surgical suture was used to secure the tendon interface of the scaffold at the supraspinatus tendon site using the Kessler suture technique. Meanwhile, a 1 mm diameter bone tunnel was drilled through the footprint, allowing the osteogenic interface of the scaffold to be anchored with the bone using surgical sutures. The incision was then closed, and all procedures were performed under sterile conditions (Fig. 8a).

2.7.3. Histological analysis of tendon-bone interface

At 8 and 16 weeks post-operatively, totally 24 animals were euthanized and samples were harvested and processed for histological and immunohistochemical analysis. The tendon and bone tissues were separately collected and used for whole transcriptome RNA sequencing analyses via Hang Zhou KaiTai Biotechnology Co., Ltd (Hangzhou, China).

3. Results

3.1. Characterization of peptides, nanofiber yarns and scaffolds

High-performance liquid chromatography (HPLC) and electrospray ionization mass spectrometry (ESI-MS) were respectively used to determine the purity and molecular weight of the synthesized peptide MDP1. The purity of MDP1 was 96.73 %, thereby indicating that the peptide can be directly used in cell experiments. Besides, multiple charged peaks were detected in the mass spectrum, including m/z 722.41 ($[M+6H]^{6+}$), 866.51 ($[M+5H]^{5+}$), and 1082.85 ($[M+4H]^{4+}$). The calculated molecular weight of the peptide was approximately 4327.5 Da, which was consistent with the theoretical value, indicating the correct structure of the synthesized peptide. The results of endotoxin test revealed that the endotoxin level of MDP1 was 0.154 EU/mg, which can be considered suitable for immune induction experiments involving macrophages (Fig. S1).

MDP1 and HA were incorporated into PLCL and SF, respectively and the surface morphology of electrospun nanofiber yarns was observed using SEM (Fig. 2a). The average diameter of fibers was 0.55 ± 0.13 μm, 0.57 ± 0.13 μm, and 0.57 ± 0.10 μm for PS, PS-M, and PS-HA groups, respectively. However, there was an insignificant difference among groups in terms of the distribution of fiber diameter (Fig. 2b and c). The thermal stability of scaffolds was further evaluated. SF, PS, PS-M, and PS-HA yarns exhibited good thermal stability within the temperature range of 30 °C–400 °C. While SF yarn without loaded with fibers displayed rapid decomposition rate, PS, PS-M, and PS-HA manifested lower decomposition rate. It is worth to note that all yarns showed a mass loss more than that of 60 % at 600 °C (Fig. 2d).

We further evaluated the degradation of scaffolds *in vitro*, which exhibited the loss of approximately 30 % of mass for up to 12 weeks. The scaffolds exhibited slow degradation rate, which may have implications for their applications *in vivo* as they can provide the mechanical strength (Fig. 2e). To evaluate the release of MDP1, nanofiber yarn loaded with Rhodamine B-grafted MDP1 (RgM) was woven into scaffolds and subjected to *in vitro* release studies (Supplementary Fig. S3). The RgM showed sustained release from scaffolds for up to 28 days *in vitro* and the value for the cumulative release was found to be 756.96 ± 28.22 μg. Similarly, HA was slowly released from scaffolds and its cumulative released amount was 319.45 ± 32.79 μg for up to day 28 *in vitro*. Since rotator cuff healing requires continuous drug release to resolve inflammatory response and promote osteogenesis, sustained and controlled release of MDP1 and HA may have implications for the applications of these scaffolds for rotator cuff repair (Fig. 2f and g).

The structural analysis of scaffolds was carried out with FTIR. The FTIR spectrum of PLCL exhibited characteristic absorption peaks at 1756 cm^{-1} and 1086 cm^{-1}, which were ascribed to the stretching vibrations of carbonyl (C=O) group and the symmetric stretching vibrations of the C–O–C bond, respectively. The absorption peaks at 1640 cm^{-1} and 1518 cm^{-1} were attributed to Amide I and Amide II bonds of the SF. On the other hand, absorption peaks appeared at 601 cm^{-1} and 558 cm^{-1} were ascribed to the $\nu 4$ bending vibrations of the phosphate (PO_4^{3-}) groups of HA. The PS, PS-M, and PS-HA scaffolds exhibited these peaks, which is indicative of the successful incorporation of PLCL, SF, and HA in the scaffolds (Fig. 2h).

The FE-SEM results further confirmed that the HA was successfully loaded into scaffolds. Elemental mapping revealed 0.75 % of phosphorous (P) in the scaffold (Supplementary Fig. S4). The PS-HA scaffolds
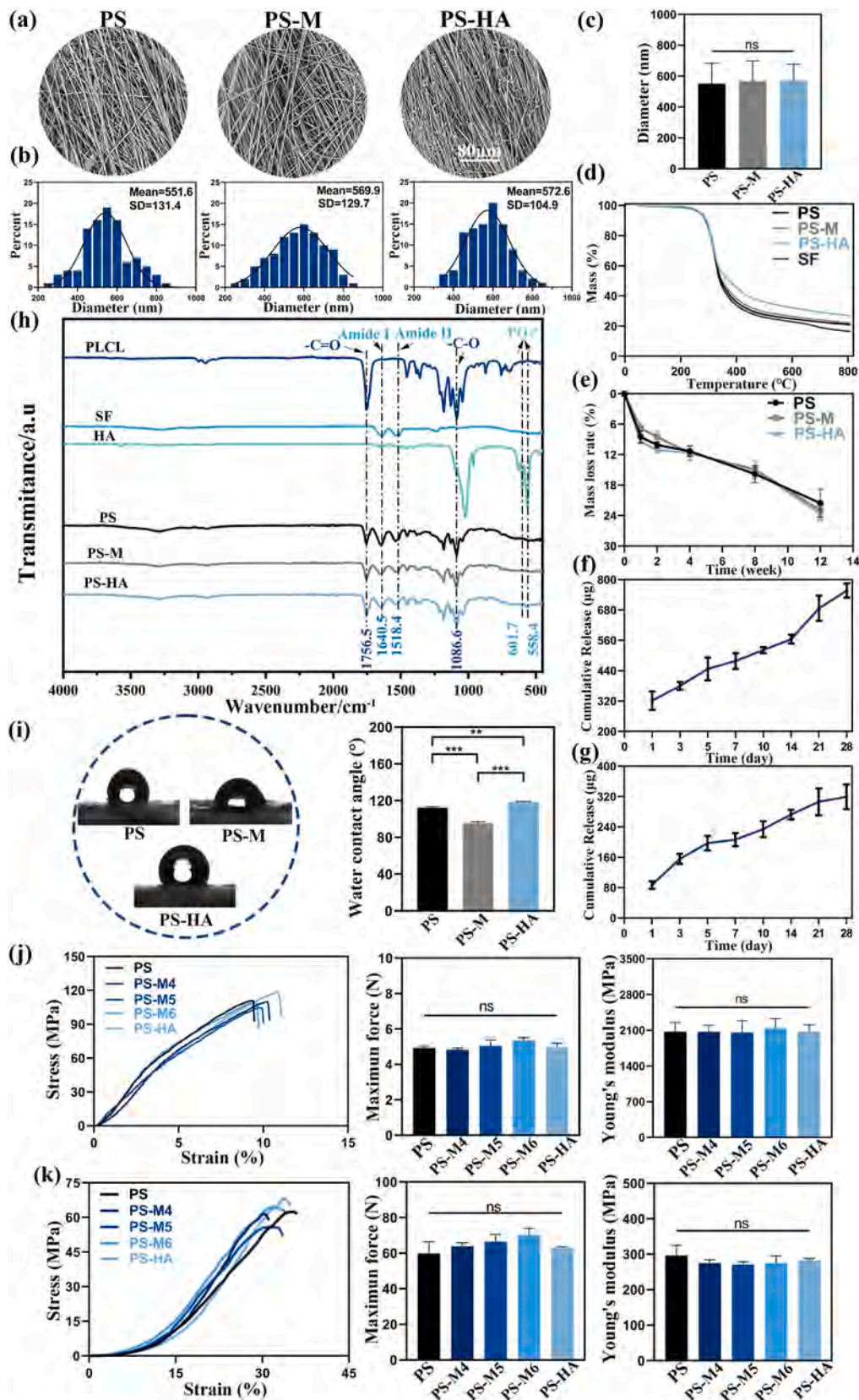
Fig. 2. Characterization of nanofiber yarns and scaffolds. (a) SEM image of nanofiber yarn: PLCL/SF (PS), PLCL/SF/MDP1 (PS-M) and PLCL/SF/HA (PS-HA). (b–c) Diameter distribution of nanofiber and comparison between groups. (d) Thermogravimetric analysis of yarns. (e) *In vitro* degradation of scaffolds for up to 12 weeks. (f) Cumulative release of MDP1 grafted with Rhodamine B for up to 28 days. (g) Cumulative release of HA for up to 28 days. (h) FTIR spectra of PLCL, SF, HA, and scaffolds. (i) Water contact angle of scaffolds. (j) Mechanical properties of nanofiber yarns. (k) Mechanical properties of scaffolds. *$P < 0.05$, **$P < 0.01$, and ***$P < 0.001$. ($n = 3$).

loaded with HA particles exhibited WCA value of 118.26 ± 0.85°, thereby indicating high hydrophobicity. On the other hand, WCA of the PS was 112.20 ± 1.0° and that of the PS-M was 95.36 ± 1.79°, which indicated higher hydrophilicity of these scaffolds than that of the PS-HA scaffold (Fig. 2i).

The mechanical properties of yarns with the inclusion of different types of fibers were evaluated albeit an insignificant difference among groups in terms of mechanical properties. Nanofiber deposition showed no significant differences, exhibiting an average maximum force of 5.03 ± 0.25 N, ultimate tensile strength of 115.51 ± 6.65 MPa, strain at failure of 10.62 ± 0.84 %, and average Young's modulus of 2085.24 ± 153.68 MPa (Fig. 2j, Supplementary Fig. S5). On the other hand, scaffolds from different groups, woven with 24 yarns using a weaving machine displayed significantly enhanced mechanical performance. The values for the average maximum force were 64.80 ± 5.06 N, average ultimate tensile strength was 59.45 ± 4.41 MPa, and average strain at failure was 35.29 ± 2.48 % (Supplementary Fig. S5), and average Young's modulus was 278.59 ± 15.47 MPa (Fig. 2k).

3.2. Anti-inflammatory and anti-oxidant effects of MDP1

MDP1 may promote immune-modulation by regulating macrophages polarization from M0 to M2 phenotypes in a manner similar to that of lncRNA MM2P. Consequently, it is important to delineate the signaling pathways and anti-inflammatory functions of MDP1 in macrophages *in vitro*. Extract solution of scaffolds loaded with different concentrations of MDP1 were utilized to assess anti-inflammatory and anti-oxidant properties (Fig. 3).

Flow cytometry analysis exhibited distinct anti-inflammatory effect of MDP1 (Fig. 3a and b). The ratio between CD206$^+$ (anti-inflammatory, M2) macrophages and CD86$^+$ (anti-inflammatory, M1) macrophages marked by M2/M1 ratio was increased with an increase in the concentration of MDP1, and attained its maximum value at 0.125 mg/mL MDP1 (PS-M4). MDP1 concentrations beyond 0.125 mg/mL (e.g., 0.25 mg/mL in PS-M5 and 0.5 mg/mL in PS-M6) exhibited a deleterious effect on macrophages polarization from M0 to M2 phenotype which was evident from a reduction in the M2/M1 value. Notably, LPS + PS-M4 group exhibited weaker anti-inflammatory activity than that of the PS-M4 but stronger than that of the PS-M5, suggesting that an appropriate concentration of MDP1 is important to reverse M1 polarization and promote M2 polarization in macrophages. PS-M6 even exhibited a pro-inflammatory effect. These results indicated the beneficial effect of the low concentration of MDP1 on immune-modulation, which may have implications to resolve inflammatory response *in vivo*.

A nonlinear dose-response effect was observed in the anti-inflammatory polarization of macrophages induced by MDP1, suggesting that macrophages stimulated with different concentrations of MDP1 may exert varying influences on the proliferation and function of tenocytes, fibrochondrocytes, and rBMSCs. Therefore, PS-M4, PS-M5, and PS-M6 were selected to delineate the peak effect, post-peak effect, and potential reversal effect, respectively.

qPCR analysis showed an increase in the expression of the anti-inflammatory interleukin-4 (IL-4) gene, while a decrease in the expression of tumor necrosis factor-alpha (TNF-α) with an increase in the MDP1 concentration. This may be attributed to the effect of MDP1 on macrophages polarization, which indirectly regulated the expression of related cytokines. Despite LPS stimulation, the LPS + PS-M4 group still exhibited relatively higher IL-4 expression and lower TNF-α expression, further demonstrating the anti-inflammatory ability of MDP1 to reverse M1 polarization in macrophages. PS-M4 has higher IL-4 expression while lower TNF-α expression than that of the control group. The expression of the pro-inflammatory gene TNF-α was increased beyond PS-M4 (e.g., PS-M5, PSM-6, etc.) (Fig. 3c).

To further explore the correlation between MDP1 and lncRNA MM2P in regulating macrophage signaling pathways, LPS containing medium and extract solution of PS-M4 scaffold were used to treat RAW264.7

macrophages for up to 30 min and analyzed using western blotting (Fig. 3d and e). The levels of p-STAT3 and p-STAT6 were significantly higher in the MDP1 group than that of the LPS group, while the levels of STAT3 and STAT6 were lower in the MDP1 group than that of the LPS group. Relative quantification analysis of p-STAT3/STAT3 and p-STAT6/STAT6 confirmed the consistency of MDP1 regulation at the transcription factor level.

Anti-oxidative activity with DCFH fluorescence staining showed the highest fluorescence intensity in LPS-induced RAW264.7 macrophages group, which is indicative of the highest ROS level among all groups. While PS, PS-M6, and PS-M5 groups showed an intermediate level of ROS values, PS-M4 group exhibited the lowest ROS level (Fig. 3f and g). PS-M4 and PS-M5 also exhibited markedly higher NO clearance rate than that of the LPS group. In contrast, PS groups manifested the lowest NO clearance rate among all groups. These results demonstrated the beneficial effects of the PS-M4 scaffold in terms of anti-inflammatory and anti-oxidative properties, which may be attributed to upregulated antioxidant-related genes and reduced oxidative stress. Unlike flavonoids or N-acetylcysteine that act as direct antioxidants, MDP1 may exert its anti-oxidative effect indirectly by activating STAT3 and STAT6 phosphorylation pathways, which promotes macrophage polarization toward the anti-inflammatory M2 phenotype [35,36].

3.3. Biocompatibility and biofunction in vitro

CCK-8 assay was used to evaluate the cytotoxicity of MDP1. Various cell types, including RAW264.7 macrophages, tenocytes, fibrochondrocytes, and rBMSCs were seeded on scaffolds containing different concentrations of MDP1 (e.g., 0 mg/mL, 0.005 mg/mL, 0.01 mg/mL, 0.05 mg/mL, 0.125 mg/mL, 0.25 mg/mL, 0.5 mg/mL, etc.) and cultured for 1, 4, and 7 days (Fig. 4). Scaffolds loaded with different concentrations of MDP1 did not exhibit a cytotoxic effect (Fig. 4a). Similarly, L929 fibroblasts were used for live/dead staining at day 3 after culture *in vitro* (Fig. S6). Extract solution of different types of scaffolds containing different concentrations of MDP1 and HA were also used to culture tenocytes. Live/dead staining revealed good cytocompatibility of all scaffolds, with tenocytes maintaining a favorable cell morphology as evaluated at day 5 (Fig. 4b).

For the preparation of conditional culture medium, scaffolds containing varying concentrations of MDP1 (0 mg/mL, 0.125 mg/mL, 0.25 mg/mL, and 0.5 mg/mL) were immersed in complete culture medium for 12 h. A complete medium containing 0.5 mg/mL LPS was used as a negative control. The conditioned medium as well as LPS-containing media were used to culture RAW264.7 macrophages. After 12 h, the supernatant from RAW264.7 macrophages was collected using filtration and was used to further culture tenocytes (Fig. 4c).

Tenocytes cultured in conditional culture medium from the LPS group produced only a negligible amount of COL I presumably due to the presence of pro-inflammatory cytokines, such as TNF-α and IL-6, in the conditional culture medium. These pro-inflammatory cytokines can activate nuclear factor kappa-light-chain-enhancer of activated B cells (NF-κB) and mitogen-activated protein kinase (MAPK) signaling pathways, and can trigger inflammatory response. Chronic inflammation may lead to a reduction in the normal physiological functions of tenocytes, including their inability to synthesize COL I. Moreover, inflammatory responses are often accompanied with increased oxidative stress, and elevated ROS levels, which can further inhibit the synthesis of COL I [37,38]. Unlike LPS group, tenocytes cultured with the conditional culture medium from the control as well as PS-M4 groups synthesized higher levels of COL I albeit a reduction in the COL I production at higher MDP1 content (e.g., PS-M6) (Fig. 4d). These findings suggested that excessively high concentrations of MDP1 may exert an opposing effect to lower concentrations, potentially influencing the M2/M1 macrophage ratio.

Quantitative analysis of the IF staining revealed that there was no significant differences in the F-actin area (%) or the number of nuclei
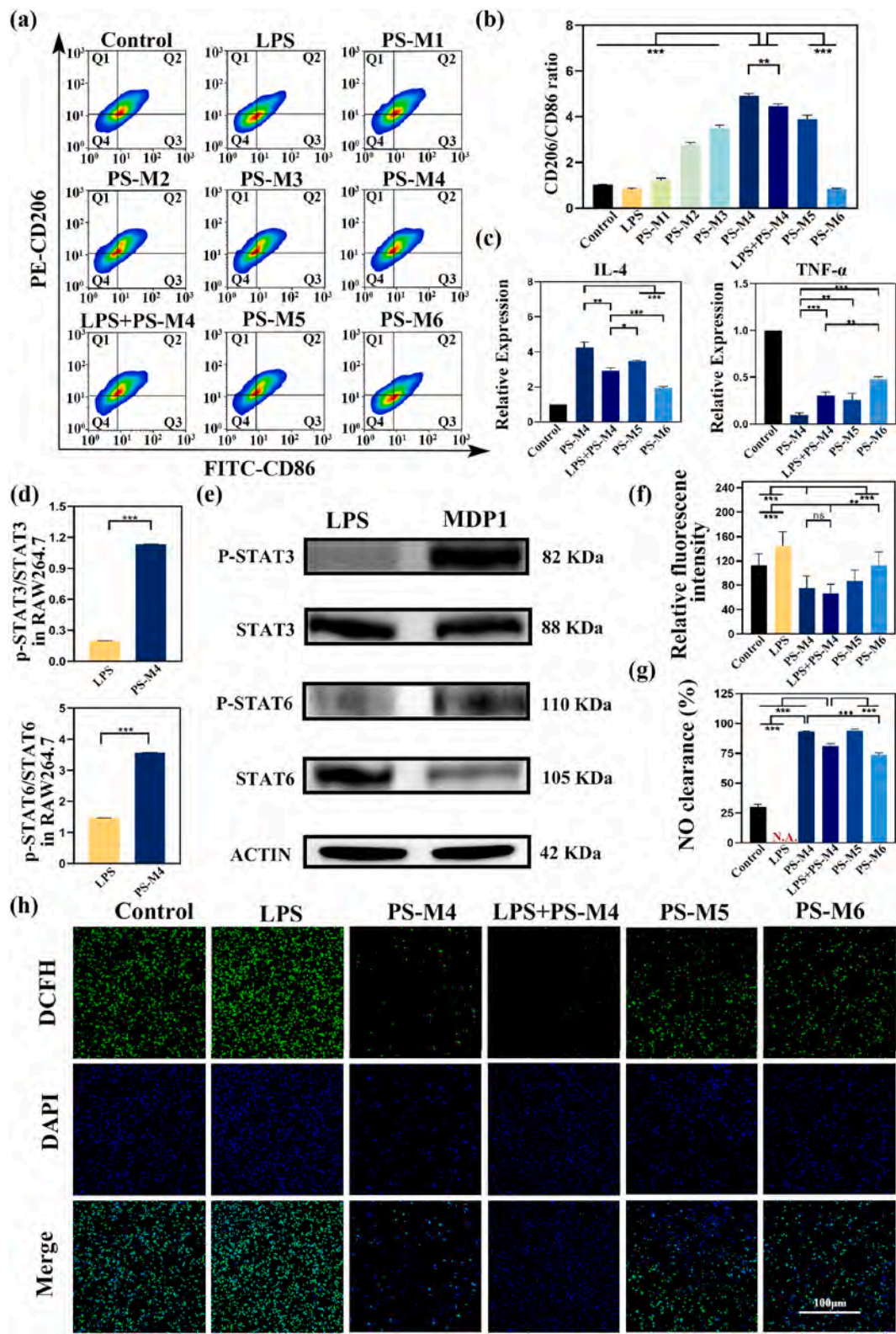
Fig. 3. Role of MDP1 in promoting macrophages polarization. (a–b) Flow cytometric analysis of RAW264.7 macrophages stimulated with the extract solution of PS-M scaffolds and lipopolysaccharide (LPS) containing medium. (c) Expression levels of IL-4 and TNF-α of RAW264.7 macrophages using qPCR. (d–e) Changes in the levels of macrophage-related transcription factors in RAW264.7 macrophages. (f–h) DCFH fluorescence staining assay, relative quantitative analysis and NO clearance rate of RAW264.7 macrophages. *P < 0.05, **P < 0.01, and ***P < 0.001. (n = 3).
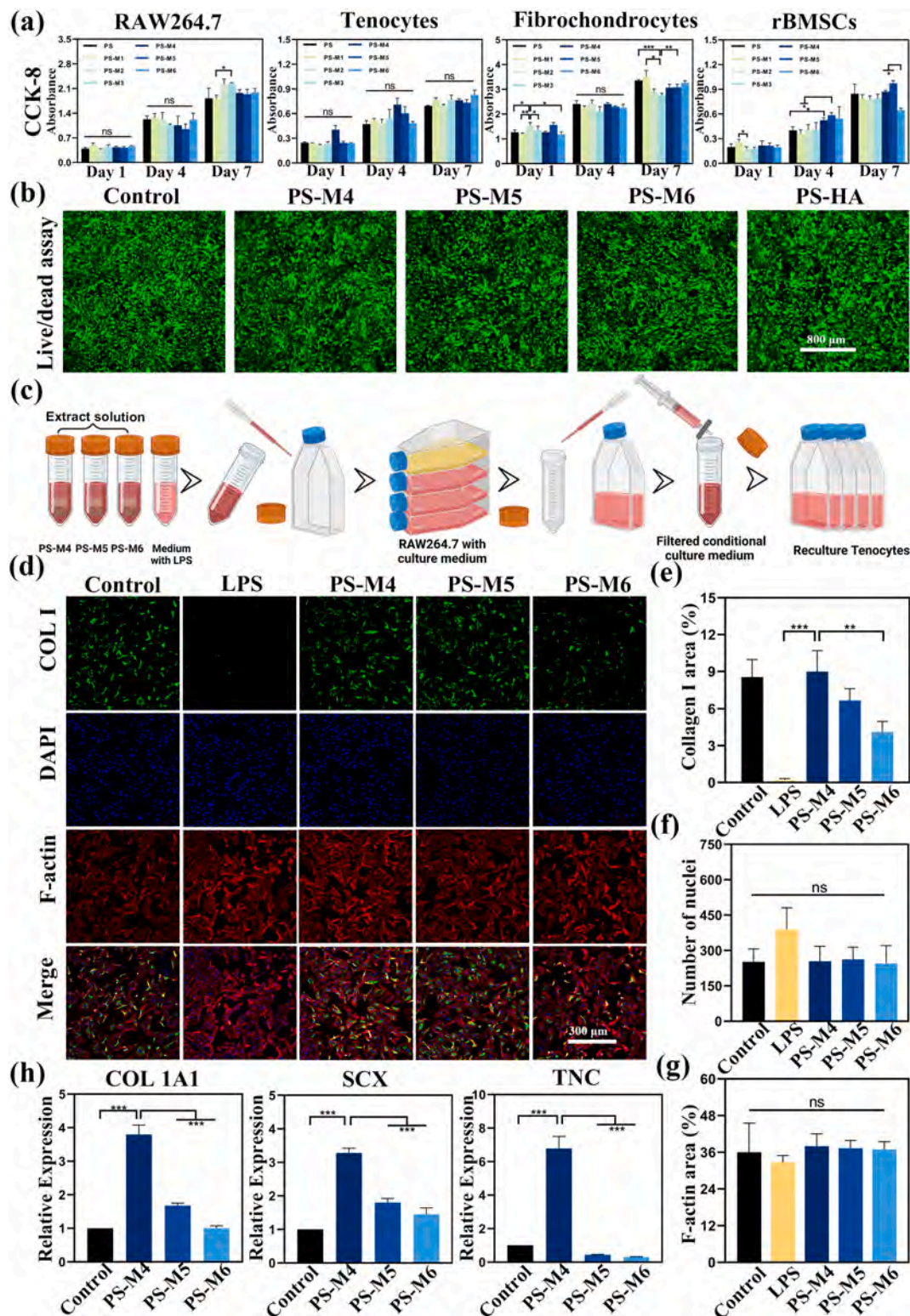
Fig. 4. Cytocompatibility of scaffolds *in vitro*. (a) Proliferation of RAW264.7 macrophages, tenocytes, fibrochondrocytes, and rBMSCs seeded on scaffolds *in vitro*. (b) Live/dead staining of tenocytes cultured along with extract solution of different types of scaffolds for up to 5 days. (c) Preparation of conditional culture medium. (d–g) Immunofluorescence (IF) staining of COL I (green), nuclei (blue) and cytoskeletal staining (red) and quantitative analysis of tenocytes cultured for 10 days. (h) Relative expression levels of COL I, SCX, and TNC in tenocytes analyzed by qPCR. *$P < 0.05$, **$P < 0.01$, and ***$P < 0.001$. ($n = 3$).

among different groups. However, PS-M4 exhibited the highest area for the COL I (8.55 ± 1.42 %) than that of the LPS group (0.2 ± 0.12 %) and PS-M6 group (4.12 ± 0.84 %). These results indicated that an appropriate concentration of MDP1 is pivotal in promoting collagen synthesis in tenocytes (Fig. 4e–g). Once tenocytes were cultured with the

conditional culture medium for up to day 5, the expression level of tendon-associated genes, including COL I, SCX, and TNC was analyzed with qPCR (Fig. 4h). PS-M4 group exhibited significantly higher expression of tendon-related genes than that of the PS-M5 and PS-M6 groups.

The conditional culture medium for tenocytes was used to further culture fibrochondrocytes (Fig. 5). PS-M4 group showed significantly higher expression of fibrocartilage-related genes, including SOX9, AGG, and COL II as compared to PS-M5 and PS-M6 groups a evaluated at day 5 of culture *in vitro* (Fig. 5b). Different conditional culture medium were used to culture fibrocartilage for 14 days, and both Alcian Blue and Safranine O staining were performed to assess the matrix synthesis activity of fibrochondrocytes (Fig. 5c–e). Since LPS-conditional medium is rich in pro-inflammatory cytokines, including TNF-α, IL-6, and IL-1β, these cytokines can suppress the normal matrix synthesis in fibrochondrocytes, particularly the synthesis of glycosaminoglycans (GAGs), such as chondroitin sulfate (CS) and keratan sulfate (KS). In addition,

prolonged inflammatory responses may lead to an increased oxidative stress and an elevated ROS level, which can reduce the content of glycoproteins in the cartilage matrix, thereby reducing the staining intensity for both Safranine O and Alcian Blue. In contrast, PS-M4 group exhibited an intense staining due to its higher content of acidic mucopolysaccharides, including CS and KS.

IF staining was performed after culturing fibrochondrocytes with the conditional medium for up to day 14 (Fig. 5f). Mirroring the IF staining results of tenocytes, the infiltration area of COL II in the LPS group was remained the lowest, at only 1.00 ± 1.06 %, indicating poor matrix synthesis activity of fibrochondrocytes in the LPS group. In contrast, the infiltration area of COL II in the PS-M4 group was the highest ($23.2 \pm$
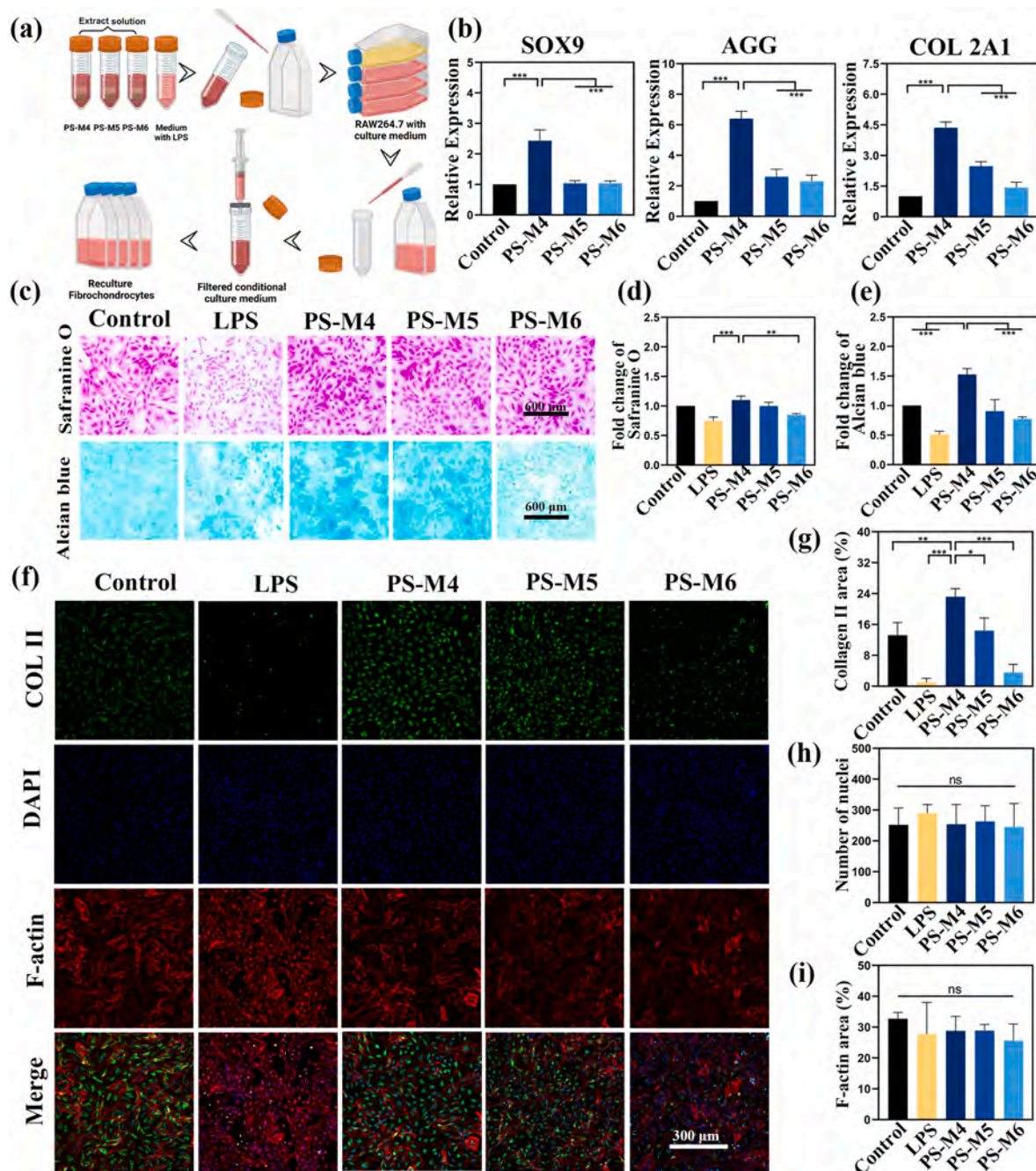

Fig. 5. Effects of scaffolds loaded with different concentrations of MDP1 on fibrochondrocytes. (a) Preparation of conditional culture medium. (b) Relative expression levels of SOX9, AGG, and collagen type II (COL II) in fibrochondrocytes analyzed by qPCR. (c–e) Safranine O, Alcian blue staining and quantitative analysis of fibrochondrocytes cultured for 14 days in conditional culture medium of scaffolds. (f–i) IF staining of COL II (green), nuclei (blue), and cytoskeletal filaments (red) and quantitative analysis of fibrochondrocytes cultured for 14 days in conditional culture medium. *$P < 0.05$, **$P < 0.01$, and ***$P < 0.001$. ($n = 3$).

2.1 %) followed by the infiltration area of the control group (13.2 ± 3.3 %) (Fig. 5g–i).

An improved level of p-STAT3 can promote the expression of SOX9. Macrophages can release exosomes containing both SOX9 mRNA and protein. Consequently, p-STAT3 and SOX9 can promote the expression of cartilage-related genes, including COL II as well as increase the synthesis of proteoglycans [23]. However, with an increase concentration of MDP1, the M2/M1 ratio in macrophages showed a decreasing trend, which may explain the gradual reduction in COL II staining in the PS-M5

and PS-M6 groups. It is worth to note that we did not observe significant difference among the groups in terms of the total number of cell nuclei and F-actin spreading area. However, it is noteworthy that the F-actin staining in the LPS group showed fluorescence signals near the cell nuclei, a phenomenon not observed in other groups. This may be attributed to prolonged inflammation and oxidative stress, which may lead to the reorganization of cytoskeletal proteins within cells [39].

Conditional as well as osteogenic induction culture media was prepared for osteogenic induction experiments (Fig. 6a). The relative
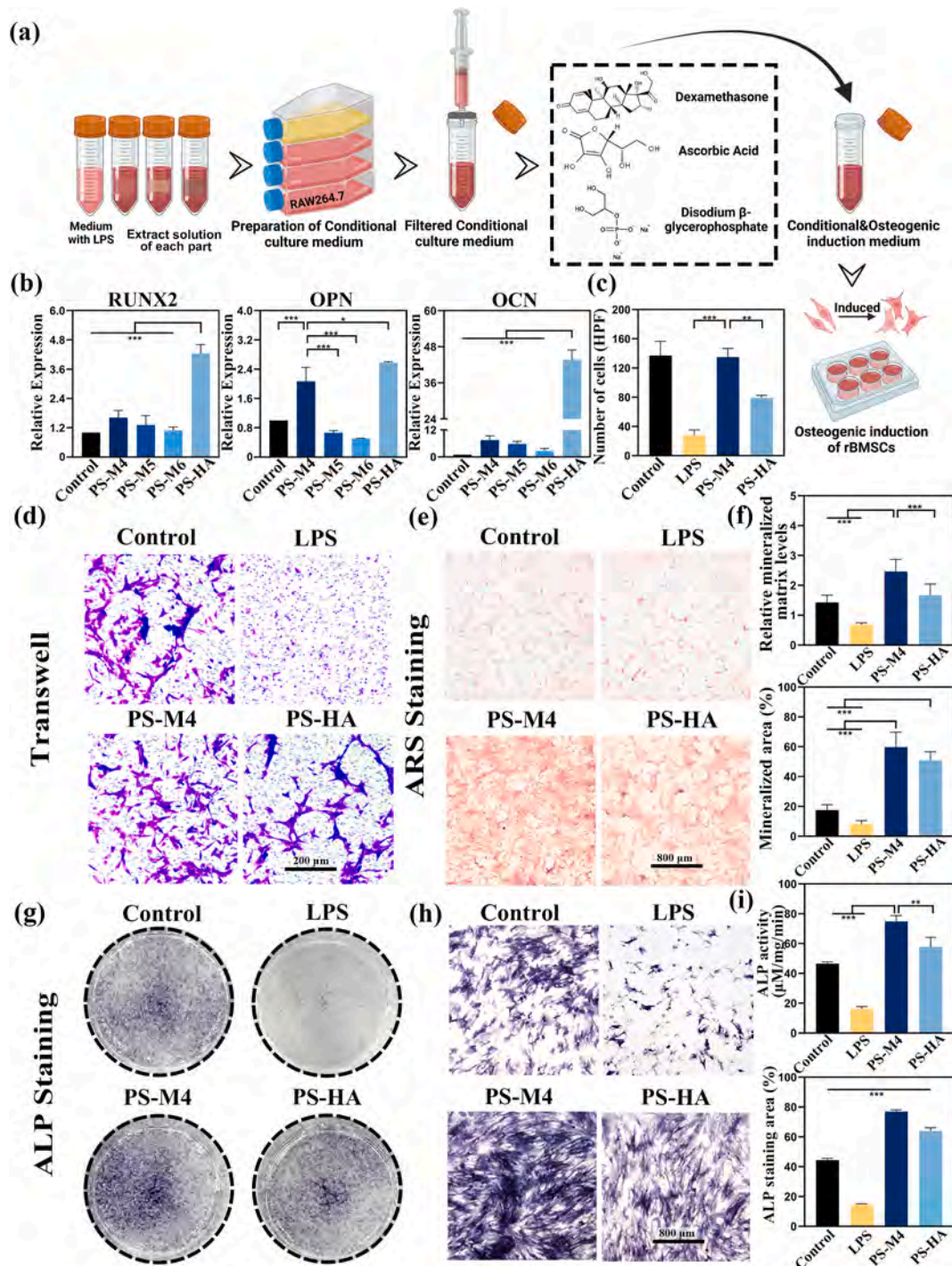

Fig. 6. Effect of MDP1 and HA on osteogenic differentiation of rBMSCs. (a) Preparation of conditional culture medium containing osteogenic induction components. (b) Relative expression levels of osteogenic-related genes, such as RUNX2, OPN, and OCN in rBMSCs, analyzed by qPCR. (c–d) Transwell migration assay of rBMSCs cultured for 12 h and its quantitative analysis. (e–f) ARS staining and relative quantification of rBMSCs. (g–i) Macroscopic image of ALP staining, magnified image (10x), and absolute quantification of rBMSCs cultured for 10 days. *P < 0.05, **P < 0.01, and ***P < 0.001. (n = 3).

expression levels of osteogenic-related genes, including RUNX2, OPN, and OCN, were analyzed by qPCR at day 5 of osteogenic induction or rBMSCs (Fig. 6b). PS-HA group exhibited significantly higher relative expression levels of osteogenic-related genes as compared to the other groups, with PS-M4 showing the second-highest expression levels of osteogenic induction. Transwell migration assay was performed to evaluate the migration of rBMSCs *in vitro* (Fig. 6c and d). Control and PS-M4 groups exhibited significantly more number of migrated cells than that of the LPS group (# of migrated cells per HPF: 137.0 ± 19.5, 135.0 ± 11.7, and 27.6 ± 7.5 cells for control, PS-M4, and LPS groups, respectively.

ARS and ALP activity assays were performed to evaluate osteogenic activity at each interface. PS-M4 group showed the highest relative mineralized matrix level, as well as mineralized area, even surpassing the PS-HA group at day 10 (Fig. 6e and f). PS-M4 group also possessed an intense purple color, indicating the highest ALP activity than that of the other groups, which is indicative of the beneficial effect of the MDP1 to promote osteogenesis (Fig. 6g–i). The PS-HA group displayed relatively high mineralization and ALP activity. In contrast, rBMSCs in the LPS group exhibited much lower mineralization and ALP activity presumably due to the prolonged inflammatory response. Inflammatory cytokines strongly inhibited osteoblast activity and related gene expression. Similarly, oxidative stress microenvironment can impair metabolism as well as bone formation ability of rBMSCs, which may lead to significantly less mineralization and ALP activity [40]. Taken together, the PS-HA group manifested an expected osteogenic effect, while the PS-M4 group outperformed the other groups in terms of osteogenic induction.

3.4. Whole transcriptome RNA sequencing analyses

The whole transcriptome RNA sequencing analysis of tendon and bone tissue was carried out to evaluate the differences in gene expression between control group and MDP1&HA scaffold group at the fourth month post-surgery (Fig. 7). As can be seen from the heatmap, principal component analysis (PCA) and differential gene genome circle map, there were significant differences between the two groups albeit a high degree of consistency within the groups (Fig. 7a &Fig. S7). As shown in the volcano plot, MDP1&HA scaffold group exhibited 273 upregulated and 164 downregulated genes related to tendon and muscle than that of the control group (Fig. 7b).

Similarly, GO enrichment analysis revealed upregulated GO terms in the MDP1&HA scaffold group than that of the control group. These upregulated GO terms were associated with tissue regeneration, anti-inflammatory response, and anti-oxidative ability, such as tendon development, neovascularization, inflammation regulation, and the removal of superoxide radicals (Fig. 7c). The chord plot further illustrated the relationship between selected GO terms and their corresponding differentially expressed genes (Fig. 7e). On the other hand, downregulated GO terms were related to the negative regulation of cell maturation and inflammatory responses, including negative regulation of cell maturation, cellular response to interleukin-17 (IL-17), and acute inflammatory response (Fig. 7d).

KEGG enrichment analysis indicated several upregulated pathways, which were primarily involved in the regulation of actin cytoskeleton, focal adhesion, apelin signaling pathway, and glutathione metabolism. In contrast, downregulated signaling pathways included, MAPK, IL-17, NOD-like receptor, and cell adhesion molecules (Fig. f, g). Mirroring tendon tissues, differences in gene expression were also evident for the bone tissue as illustrated through the heatmap, PCA and differential gene genome circle map (Fig. 7h & Fig. S6). As compared to the control group, MDP1&HA scaffold group exhibited 910 upregulated and 164 downregulated genes related to bone (Fig. 7i).

Similarly, GO enrichment analysis revealed several upregulated GO terms in the MDP1&HA scaffold group in comparison to the control group, which were primarily associated with bone mineralization, cartilage development, and ossification, regulation of bone

mineralization, and cartilage development (Fig. 7j). The chord plot further displayed the relationship between selected GO terms and their corresponding differentially expressed genes, while the GO terms related to the tendon-bone interface were highlighted in the red colour (Fig. 7l). In contrast, downregulated GO terms were mainly associated with acute/chronic inflammation and bone resorption, such as acute inflammatory response to antigenic stimulus, positive regulation of chronic inflammatory response, and regulation of bone resorption (Fig. 7k).

KEGG enrichment analysis revealed that the upregulated pathways were primarily involved in proteoglycans, cysteine and methionine metabolism, steroid hormone biosynthesis, and glycerophospholipid metabolism. On the other hand, downregulated pathways included NF-κB signaling pathway, inflammatory mediator regulation of transient receptor potential (TRP) channels, arachidonic acid metabolism, and MAPK signaling pathway (Fig. 7m and n). Taken together, these results indicated that the implantation of functionally graded scaffold can effectively modulate an excessive inflammatory environment at the tendon-bone interface while simultaneously promoting the regeneration of tendon, fibrocartilage, and bone. Therefore, these findings may have implications for the integration of the tendon-bone interface and can contribute to improved tissue repair and functional recovery.

3.5. Biocompatibility in vivo

The surgical steps for establishing the rotator cuff tear model are shown in Fig. 8a. Histological analysis was carried out to delineate the beneficial effect of functionally graded scaffold on rotator cuff healing and tendon-bone tissue regeneration. The tendon tissue, fibrocartilage layer, and bone interface are labeled as T, F, and B respectively. Fig. S8 shows overall images of the stained tissues. H&E staining was used to evaluate tissue healing at tendon-bone interface at 2M and 4M (Fig. 8b). The control group and PS scaffold group exhibited disorganized fibrocartilage interfaces and irregular bone integration at 2M. On the other hand, MDP1&HA scaffold group exhibited well-organized collagen regeneration along with distinct tissue boundaries. Masson's trichrome staining also revealed similar trends: the control and PS scaffold groups still displayed irregular and potentially degenerative fibrocartilage layers at 4M, whereas the MDP1&HA scaffold group showed more natural tissue transitions (Fig. 8c).

Safranin O/Fast Green staining was used to assess fibrocartilage regeneration, where a dense and regular fibrocartilage layer is essential for the biomechanical stability [41]. As shown in Fig. 8d, the control group exhibited severely compromised repair at 2M, with no improvement even by 4M. This poor regeneration in the control group may be ascribed to a persistent inflammation and tendon degeneration. While PS scaffold group outperformed the control group at 2M, it showed an insignificant effect than that of the control group by 4M, presumably due to severe immune reactions triggered by the bulk implant. MDP1&HA scaffold group outperformed control and PS scaffold group in terms of tissue regeneration and exhibited a well-organized and a regular tissue interface at all timepoints.

Picro-Sirius Red staining exhibited the highest collagen-positive area at 2M and 4M in the MDP1&HA scaffold group (Figs. 8e and 9a). On the other hand, in the control and PS scaffold groups, chronic inflammatory microenvironment led to the replacement of COL I with COL III during tendon-bone interface repair, thereby resulting in scar tissue formation. These scar tissues can compromise the biomechanical performance of the regenerated tissue [42].

While moderate inflammation is essential for the clearance of the debris as well as tissue regeneration, excessive inflammatory responses may adversely affect healing outcomes [43,44]. IHC staining was employed to delineate inflammatory response in implanted groups. The control group showed fewer CD206$^+$ area at 4-months (4M) than that of the 2-months (2M), which was accompanied with a marginal decrease in IL-6$^+$ area, and is suggestive of only a partial inflammation resolution
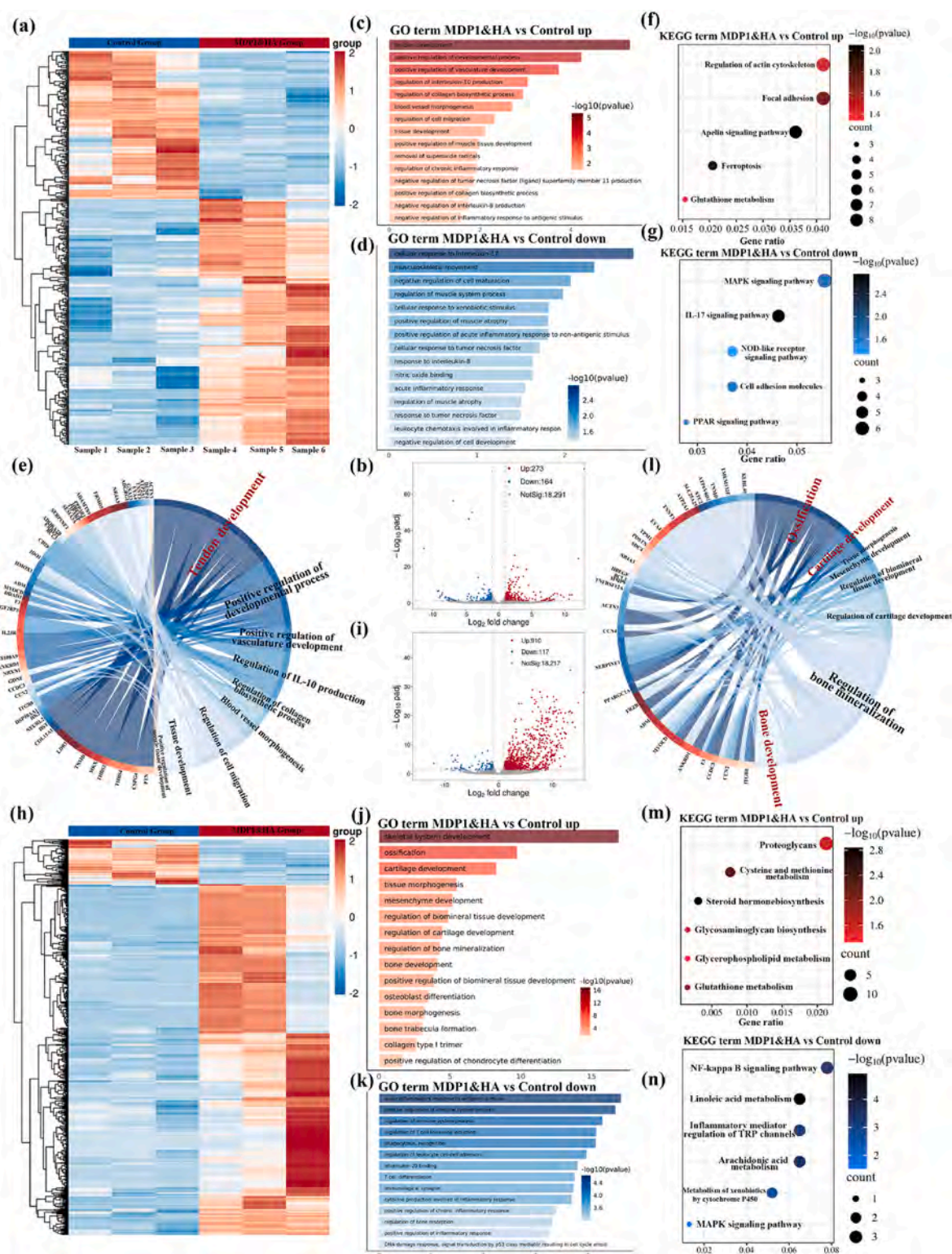
Fig. 7. Whole transcriptome RNA sequencing analysis of tendon and bone tissue at the fourth month. (a–b) Heatmap of upregulated and downregulated muscle-tendon-related genes and volcano plot of differentially expressed genes in the control group and the MDP1&HA scaffold group. (c–e) Gene Ontology (GO) enrichment analysis showing top 15 upregulated and downregulated terms along with a partial GO chord plot. (f–g) Kyoto Encyclopedia of Genes and Genomes (KEGG) enrichment analysis presenting the top 5 upregulated and downregulated pathways (h–i) Heatmap of upregulated and downregulated bone-related genes and volcano plot of differentially expressed genes in the control group and the MDP1&HA scaffold group. (j–l) GO enrichment analysis displaying the top 15 upregulated and downregulated terms, accompanied by a partial GO chord plot. (m–n) KEGG enrichment analysis illustrating the top 6 upregulated and downregulated pathways.
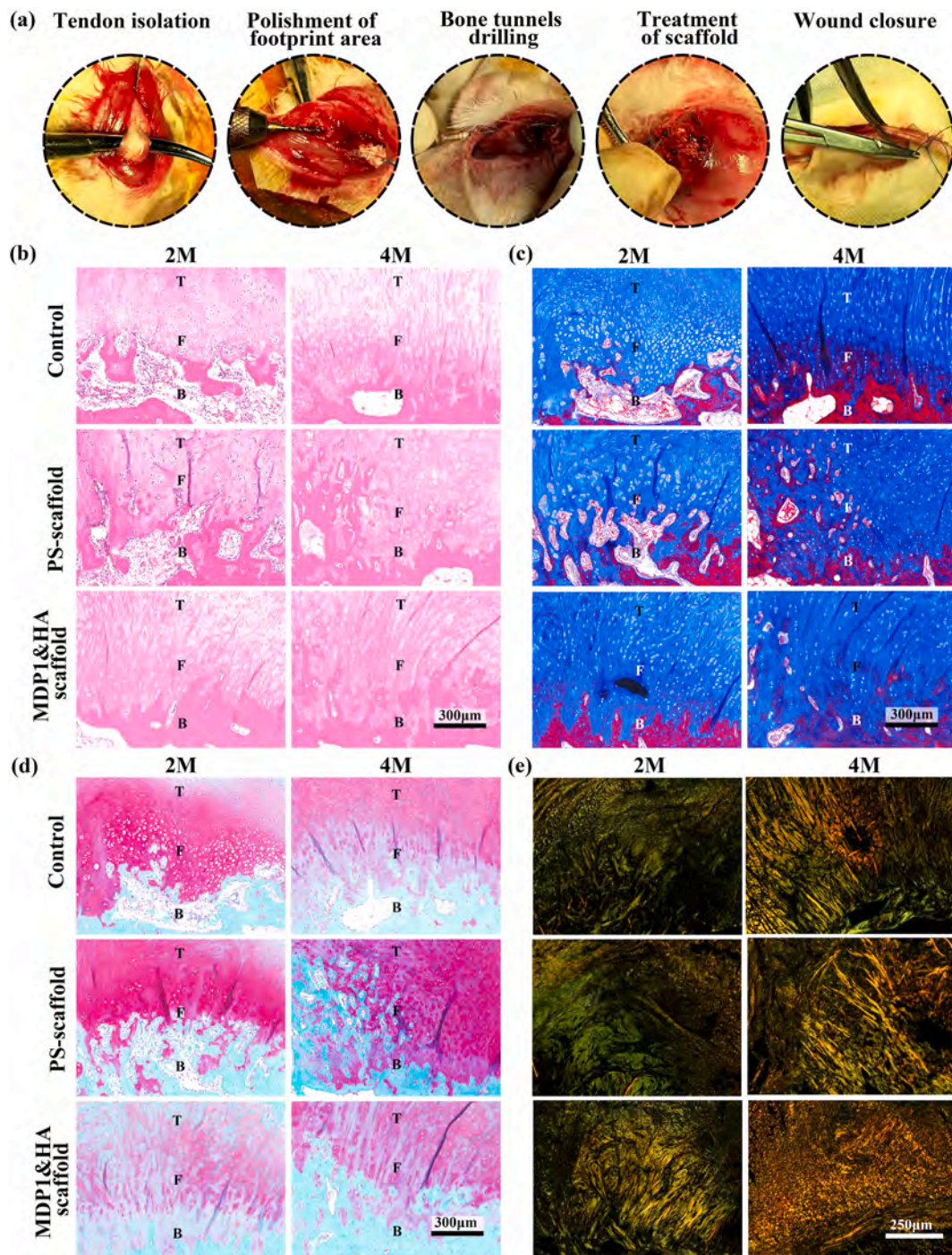
Fig. 8. Histological analysis of tendon-bone interface repair in New Zealand rabbits. (a) Schematic illustration of rotator cuff tear model. (b) Hematoxylin and eosin (H&E) staining of different groups 2 months (2M) and 4 months (4M) post-operatively. (c) Masson's trichrome staining of all groups at 2M and 4M. (d) Safranin O/ Fast Green staining of all groups at 2M and 4M and (e) Picro-Sirius Red staining under polarized light of all groups at 2M and 4M. *$P < 0.05$, **$P < 0.01$, and ***$P < 0.001$. ($n = 3$).

(Fig. 9b–c, h-i). While PS scaffold group showed a slight increase in CD206$^+$ area, it failed to resolve an overall inflammation. MDP1&HA scaffold group displayed the highest CD206$^+$ area, which was increased over an implantation time from 2M to 4M alongside the reduction of IL-6$^+$. These results indicated the beneficial effect of MDP1&HA scaffold to suppress pathological inflammation at the healing interface. IF staining analysis further revealed significantly greater COL II area in the MDP1&HA scaffold group, which is indicative of its pro-regenerative effect on fibrocartilage layer restoration (Fig. 9d–j).

We further ascertained biomechanical properties of regenerated

tissues. MDP1&HA scaffold group showed a significant increase in the mechanical performance than that of the control group as shown by the higher maximum force, Young's modulus, ultimate tensile strength (UTS), and strain at failure. In contrast, the control group displayed markedly inferior mechanical properties than that of the native bone tissues presumably due to unresolved inflammation (Fig. e–g).

Taken together, the control and PS scaffold groups exhibited suboptimal repair outcomes, characterized by disorganized collagen architecture and chaotic tissue interfaces, which may be ascribed to a persistent inflammatory cascade. MDP1&HA scaffold group effectively
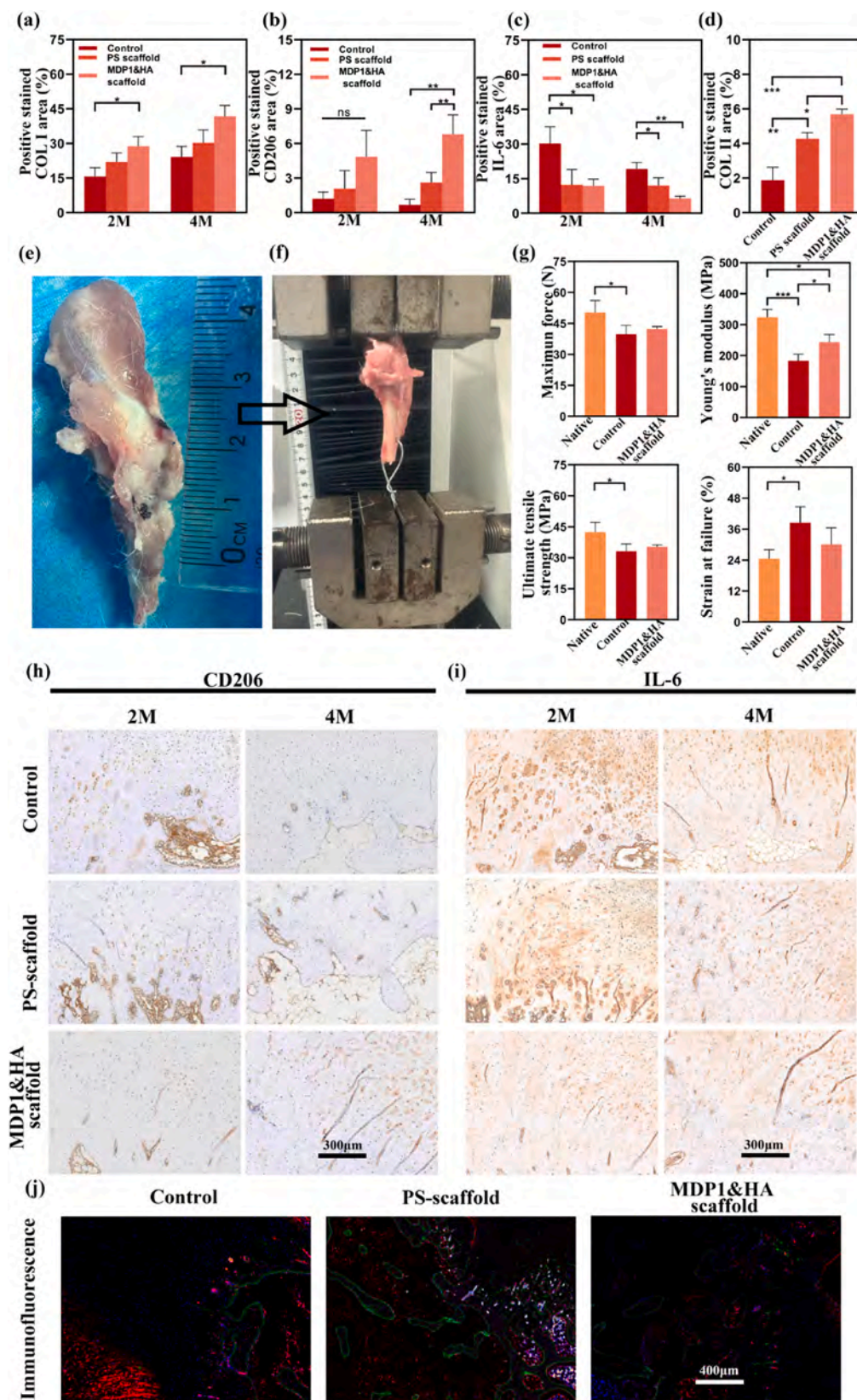
Fig. 9. Anti-Inflammatory efficacy and biomechanical evaluation of rotator cuff tear repair. (a) Quantitative analysis of COL I with Picro-Sirius Red staining. (b, h) Representative immunohistochemical (IHC) staining of CD206 and corresponding quantitative analysis of all groups at 2M and 4M. (c, i) IHC staining of IL-6 and quantitative analysis of all groups at 2M and 4M. (d, j) IF staining of COL II (green), COL I (red), and DAPI (blue) with quantitative evaluation of COL II. (e–f) Rotator cuff tissue with scaffold and biomechanical assay. (g) Biomechanical properties of rotator cuff tear model. *$P < 0.05$, **$P < 0.01$, and ***$P < 0.001$. ($n = 3$).

mitigated pathological inflammation and promoted the regeneration of a structurally organized interface. The MDP1&HA scaffold also exhibited the regeneration of well-aligned aligned COL II fibers, which were anchored to the bone tissue. This orchestrated healing process may not only prevent tendon calcification and fibrocartilage degeneration but may also restore biomechanical properties to the levels comparable to native tendon-bone interface.

4. Discussions

This study developed a functionally graded electrospun scaffold to address challenges of tendon-bone interface regeneration for rotator cuff repair. To overcome post-operative re-tearing risks associated with inadequate healing, the scaffold combines enhanced mechanical performance with its hierarchical microstructure optimized for enhanced cellular infiltration. The design incorporates MDP1 in the fibrocartilage-mimetic region to induce macrophages polarization towards M2 phenotype as well as regulate growth factor expression. On the other hand, the inclusion of HA can promote osteointegration at the bone tissue interface. Both *in vitro* and *in vivo* results showed the beneficial effect of the scaffold in modulating inflammatory micro-environments and promoting biointerface regeneration. This multidimensional repair strategy may therefore offer a new paradigm for tendon-bone interface reconstruction. The native rotator cuff tendon-bone interface exhibits a complex transitional architecture with distinct requirement of mechanical properties (e.g., an E value of 200 MPa for the tendon), unmineralized fibrocartilage, mineralized fibrocartilage, bone (an E value of 20 GPa) [45,46]. This gradient structure enables critical mechanical buffering through fibrocartilage layer and prevents stress concentration and tissue damage under tensile loading [47].

For patients with rotator cuff tears, particularly those with full-thickness tears, post-traumatic inflammatory cascade coupled with oxidative stress activation drives tenocyte apoptosis, fibrotic transformation, and ECM disorganization [48–50]. This pathophysiological progression ultimately leads to scar tissues with mechanical properties inferior to the native tendon tissues [51]. Moreover, this scar tissue-mediated healing fails to recapitulate anatomically precised reattachment of tendon-to-bone insertion since the disorganized ECM architecture, characterized by an excessive deposition of COL III may not recapitulate the structural hierarchy or load-bearing capacity of native tissues [42]. Consequently, bioactive scaffolds featuring heterogeneous soft–hard architectures or incorporating small-molecule functional agents-such as anti-inflammatory, anti-oxidative, osteogenic, chondrogenic, or angiogenic compounds-may offer a promising strategy to modulate the pathological microenvironment and facilitate functional interface regeneration [52,53].

Bioactive scaffolds with functional gradation or heterogeneous structures have become one of the main focus in current research on rotator cuff tendon-to-bone interface repair and ligament regeneration [54]. Inspired by the work of Mo et al., who developed a hand-woven scaffold with a continuous mineral gradient to control spatial mineral distribution, our study seeks to complement this approach by incorporating a computer-aided weaving strategy for improved structural regularity [55]. Furthermore, by integrating immunomodulatory biofunctionalization, we aim to introduce additional biochemical regulation. In particular, a novel peptide, MDP1, was incorporated to actively modulate the immune microenvironment, which represents a distinct advancement beyond purely structural optimization of scaffolds for rotator cuff tear repair. This combined strategy may facilitate multiple repair pathways, including fibrocartilage formation and osseointegration, thereby contributing to the ongoing efforts toward more effective and multifunctional rotator cuff interface regeneration. Wu et al. developed a multiphasic bone-ligament-bone scaffold by combining functionalized PLA and fiber yarns for anterior cruciate ligament (ACL) reconstruction [56]. Although their scaffold design is more suited to the symmetrical characteristics of ligament repair, the concept of a heterogeneous bioactive scaffold with a soft-hard interface has provided valuable inspiration for constructing scaffolds that more closely mimic the intrinsic complexity of the tendon-bone interface.

Beyond the focus on functional gradation and heterogeneous architectures, the incorporation of anti-inflammatory and anti-oxidative agents into scaffolds has also emerged as a key strategy. This is especially relevant in rotator cuff injuries, where regenerative outcome is often hindered by an excessive inflammatory milieu. Modulation of the local immune response through bioactive components is therefore considered critical to improving repair efficacy. Notable examples include tannic acid-modified decellularized tendon scaffolds, which mitigate ROS-mediated fibrosis [18], Wnt3a-functionalized nanofiber, which promoted M2 macrophage polarization via Wnt/β-catenin signaling, and 3D-printed biomimetic scaffolds incorporating spatially organized stem cells with immunomodulatory nanoparticles (NPs) [20, 57].

Our study integrates two prevailing scaffold design strategies for tissue repair-functional gradation and the incorporation of small-molecule bioactive agents-while addressing some of their respective limitations. We developed a textile-inspired solution based on dual-spray electrospun silk fibroin (SF) nanofiber yarns to construct a functionally graded triphasic scaffold that mimics the hierarchical structure of the tendon-fibrocartilage-bone interface. This design combines nanofibrous networks that facilitate cell adhesion with strategically engineered inter-yarn spaces to support neo-tissue ingrowth, thereby enabling region-specific interface regeneration. MDP1 was incorporated into scaffolds to modulate fibrocartilage interface regeneration, which can promote cartilage differentiation via STAT3/STAT6 phosphorylation [23,40,58]. Similarly, HA-mediated release of calcium and phosphate ions can be beneficial to promote osteogenesis at tendon-to-bone interface through enhanced mineralization as well as osteogenic differentiation of BMSCs [59,60]. This integrated strategy therefore optimizes the biomechanical performance of the tendon-bone interface as well as an overall rotator cuff healing.

This study also has several limitations. First, MDP1, an anti-inflammatory peptide, was screened and synthesized for the first time based on the open reading frame of lncRNA MM2P. Our current investigation has only provided preliminary insights into anti-inflammatory and anti-oxidative properties of MDP1 alongside its potential to regulate downstream signaling pathways. Notably, the observed concentration-dependent biphasic effect of MDP1 during experiments is an intriguing phenomenon, which warrants further in-depth exploration. Additionally, at the molecular level, while MDP1 appears to exert similar effects on the signal transducer and activator of transcription (STAT) pathways as that of the lncRNA MM2P, the potential regulatory relationship between MDP1 and lncRNA MM2P remains unknown and requires further clarification.

On the macroscopic level, the scaffold design also presents certain limitations. First, because the scaffold is composed of SF yarns coated with electrospun nanofibers, its overall thickness cannot be significantly reduced. To ensure sufficient mechanical support at the tendon–bone interface, the scaffold must meet specific width and length requirements, leading to a relatively large implant volume. While yarn surfaces are coated with highly biocompatible polymers, such as SF, bulky structure may provoke an inflammatory response, which may shorten implant's lifespan [61].

Second, while *in vivo* experiments were carried out for up to 16 weeks, the implanted scaffolds were not fully degraded, which necessitates further optimization of implant material to enable biodegradation of scaffold well-commensurate with tissue regeneration. Third, the PS group was not included in the biomechanical testing *in vivo*. While PS scaffold group exhibited improved mechanical strength compared to the control group, it did not show a statistically significant difference from the MDP1&HA group. Therefore, to more clearly demonstrate the unique therapeutic benefits of MDP1, the PS group was instead included in the histological and immunohistochemical analyses.

Finally, although the scaffold is broadly categorized as functionally graded, mechanical properties across its three distinct regions remain largely uniform. This means that it still falls short of precisely mimicking the heterogeneous biological and mechanical characteristics of the native tendon–fibrocartilage–bone interface, thereby increasing the risk of premature failure under physiological loading. Despite these limitations, MDP1-loaded functionally graded scaffold remains a promising and adaptable strategy for rotator cuff repair. By integrating anti-inflammatory and antioxidant functions, multi-lineage differentiation capacity, and mechanical support, this scaffold adopts a multidimensional approach to promote effective regeneration of the complex tendon–bone interface.

5. Conclusion

A functionally graded scaffold was successfully developed to address the high re-tear rate of rotator cuff injuries following arthroscopic surgery. The scaffold was fabricated using woven nanofiber yarns loaded with MDP1, a peptide derived from lncRNA MM2P, and HA, enabling biomimetic reconstruction of tendon, fibrocartilage, and bone interfaces *in vivo*. By integrating anti-inflammatory, antioxidant, and bioactive properties, the scaffold facilitates tissue infiltration and promotes functional integration at the tendon-bone interface. The therapeutic potential of scaffolds was further evaluated *in vivo* using a rabbit model. Scaffold co-loaded with MDP1 and HA manifested distinct improvement in regenerative outcomes as compared to the control and PS scaffold groups, with no evidence of cartilage degradation or tendon calcification. Given an outstanding *in vivo* reparative efficacy of this functionally graded scaffold, it may offer a promising solution the management of severe rotator cuff tears and potentially other related disciplines.

CRediT authorship contribution statement

Hao Feng: Writing – review & editing, Writing – original draft, Validation, Software, Resources, Project administration, Methodology, Formal analysis, Data curation, Conceptualization. **Gonghao Zhang:** Writing – review & editing, Validation, Resources. **Li Xiong:** Validation, Resources, Methodology. **Panpan Shang:** Funding acquisition. **Xiao Yu:** Visualization, Project administration. **Bin Chai:** Supervision. **Lu Han:** Resources. **Shuqi Lou:** Software. **Muhammad Shafiq:** Writing - original draft, Writing - reviewing & editing, Formal analysis. **Yiying Zhang:** Methodology. **Mohamed EL-Newehy:** Funding acquisition, Software, Supervision. **Meera Moydeen Abdulhameed:** Methodology, Resources, Supervision. **Zhengchao Yuan:** Writing – review & editing, Writing – original draft, Methodology. **Xiumei Mo:** Writing – review & editing, Project administration, Funding acquisition. **Yunhan Ji:** Writing – review & editing, Resources, Formal analysis, Conceptualization.

Data availability

Data will be made available on request.

Ethics approval and consent to participate

All animal experiments were carried out in accordance with the guidelines approved by the Animal Ethics Committee of Shanghai Tongren Hospital (A2024-031-01).

Declaration of competing interest

The authors declare that they have no known competing financial interests or personal relationships that could have appeared to influence the work reported in this paper.

Appendix A. Supplementary data

Supplementary data to this article can be found online at https://doi.org/10.1016/j.bioactmat.2025.06.032.

References

[1] A. Bedi, J. Bishop, J. Keener, D.A. Lansdown, O. Levy, P. MacDonald, N. Maffulli, J. H. Oh, V.J. Sabesan, J. Sanchez-Sotelo, R.J. Williams 3rd, B.T. Feeley, Rotator cuff tears, Nat. Rev. Dis. Primers 10 (2024) 8.
[2] Y. Chen, Y. Li, W. Zhu, Q. Liu, Biomimetic gradient scaffolds for the tissue engineering and regeneration of rotator cuff enthesis, Biofabrication 16 (2024) 032005.
[3] C. Zhu, J. Qiu, S. Thomopoulos, Y. Xia, Augmenting tendon-to-bone repair with functionally graded scaffolds, Adv. Healthcare Mater. 10 (2021) e2002269.
[4] J.H. Ji, Y.Y. Kim, K. Patel, N. Cho, S.E. Park, M.S. Ko, S.J. Park, J.O. Kim, Dexamethasone facilitates nf-kappab signal pathway in tnf-alpha stimulated rotator cuff tenocytes, J. Microbiol. Biotechnol. 29 (2019) 297–303.
[5] W.H. Lee, H.K. Do, J.H. Lee, B.R. Kim, J.H. Noh, S.H. Choi, S.G. Chung, S.-U. Lee, J. E. Choi, S. Kim, M.J. Kim, J.-Y. Lim, Clinical outcomes of conservative treatment and arthroscopic repair of rotator cuff tears: a retrospective observational study, Ann. Rehabil. Med. 40 (2016) 252–262.
[6] C. Chen, Q. Shi, M. Li, Y. Chen, T. Zhang, Y. Xu, Y. Liao, S. Ding, Z. Wang, X. Li, C. Zhao, L. Sun, J. Hu, H. Lu, Engineering an enthesis-like graft for rotator cuff repair: an approach to fabricate highly biomimetic scaffold capable of zone-specifically releasing stem cell differentiation inducers, Bioact. Mater. 16 (2022) 451–471.
[7] A. Mandaleson, re-tears after rotator cuff repair: current concepts review, J. Clini. Orthopaed. Trauma 19 (2021) 168–174.
[8] A.G. Schwartz, J.D. Pasteris, G.M. Genin, T.L. Daulton, S. Thomopoulos, Mineral distributions at the developing tendon enthesis, PLoS One 7 (2012) e48630.
[9] H.H. Lu, S. Thomopoulos, Functional attachment of soft tissues to bone: development, healing, and tissue engineering, Annu. Rev. Biomed. Eng. 15 (2013) 201–226.
[10] A.C. Deymier-Black, J.D. Pasteris, G.M. Genin, S. Thomopoulos, Allometry of the tendon enthesis: mechanisms of load transfer between tendon and bone, J. Biomech. Eng. 137 (2015) 111005.
[11] C.T. Thorpe, M.J. Peffers, D. Simpson, E. Halliwell, H.R. Screen, P.D. Clegg, Anatomical heterogeneity of tendon: fascicular and interfascicular tendon compartments have distinct proteomic composition, Sci. Rep. 6 (2016) 20455.
[12] C.T. Thorpe, H.L. Birch, P.D. Clegg, H.R. Screen, The role of the non-collagenous matrix in tendon function, Int. J. Exp. Pathol. 94 (2013) 248–259.
[13] M.J. Buehler, Nature designs tough collagen: explaining the nanostructure of collagen fibrils, Proc. Natl. Acad. Sci. 103 (2006) 12285–12290.
[14] X. Yu, Y. Shen, J. Cui, Y. Ding, Y. Morsi, B. Sun, X. Mo, H. Gu, The potential application of electrical stimulation in tendon repair: a review, Med-X 3 (2025) 7.
[15] L. Rossetti, L.A. Kuntz, E. Kunold, J. Schock, K.W. Muller, H. Grabmayr, J. Stolberg-Stolberg, F. Pfeiffer, S.A. Sieber, R. Burgkart, A.R. Bausch, The microstructure and micromechanics of the tendon-bone insertion, Nat. Mater. 16 (2017) 664–670.
[16] J.-Y. Rho, L. Kuhn-Spearing, P. Zioupos, Mechanical properties and the hierarchical structure of bone, Med. Eng. Phys. 20 (1998) 92–102.
[17] C.N. Maganaris, J.P. Paul, In Vivo Human Tendon Mechanical Properties, Wiley Online Library, 1999.
[18] L.L. Zhao, J.J. Luo, J. Cui, X. Li, R.N. Hu, X.Y. Xie, Y.J. Zhang, W. Ding, L.J. Ning, J. C. Luo, T.W. Qin, Tannic acid-modified decellularized tendon scaffold with antioxidant and anti-inflammatory activities for tendon regeneration, ACS Appl. Mater. Interfaces 16 (2024) 15879–15892.
[19] J.Y. Sunwoo, C.D. Eliasberg, C.B. Carballo, S.A. Rodeo, The role of the macrophage in tendinopathy and tendon healing, J. Orthop. Res. 38 (2020) 1666–1675.
[20] Y. Wei, X. Yun, Y. Guan, S. Cao, X. Li, Y. Wang, H. Meng, Y. Liu, Q. Quan, M. Wei, Wnt3a-modified nanofiber scaffolds facilitate tendon healing by driving

macrophage polarization during repair, ACS Appl. Mater. Interfaces 15 (2023) 9010–9023.

[21] J. Cao, R. Dong, L. Jiang, Y. Gong, M. Yuan, J. You, W. Meng, Z. Chen, N. Zhang, Q. Weng, H. Zhu, Q. He, M. Ying, B. Yang, Lncrna-mm2p identified as a modulator of macrophage m2 polarization, Cancer Immunol. Res. 7 (2019) 292–305.

[22] K. Peng, C. Biao, Y.Y. Zhao, L.C. Jun, W. Wei, A.B.L.Z. Ylnyz, L. Song, Long non-coding rna mm2p suppresses m1-polarized macrophages-mediated excessive inflammation to prevent sodium taurocholate-induced acute pancreatitis by blocking shp2-mediated stat3 dephosphorylation, Clin. Exp. Med. 23 (2023) 3589–3603.

[23] J. Bai, Y. Zhang, X. Zheng, M. Huang, W. Cheng, H. Shan, X. Gao, M. Zhang, L. Sheng, J. Dai, Y. Deng, H. Zhang, X. Zhou, Lncrna mm2p-induced, exosome-mediated transfer of sox9 from monocyte-derived cells modulates primary chondrocytes, Cell Death Dis. 11 (2020) 763.

[24] T.P. LaBranche, M.I. Jesson, Z.A. Radi, C.E. Storer, J.A. Guzova, S.L. Bonar, J. M. Thompson, F.A. Happa, Z.S. Stewart, Y. Zhan, C.S. Bollinger, P.N. Bansal, J. W. Wellen, D.P. Wilkie, S.A. Bailey, P.T. Symanowicz, M. Hegen, R.D. Head, N. Kishore, G. Mbalaviele, D.M. Meyer, JAK inhibition with tofacitinib suppresses arthritic joint structural damage through decreased rankl production, Arthritis Rheum. 64 (2012) 3531–3542.

[25] K. Zhou, P. Yu, X. Shi, T. Ling, W. Zeng, A. Chen, W. Yang, Z. Zhou, Hierarchically porous hydroxyapatite hybrid scaffold incorporated with reduced graphene oxide for rapid bone ingrowth and repair, ACS Nano 13 (8) (2019) 9595–9606.

[26] Y. Chen, X. Dong, M. Shafiq, G. Myles, N. Radacsi, X. Mo, Recent advancements on three-dimensional electrospun nanofiber scaffolds for tissue engineering, Adv. Fiber Mater. 4 (5) (2022) 959–986.

[27] X. Xie, Y. Chen, X. Wang, X. Xu, Y. Shen, A.u.R. Khan, A. Aldalbahi, A.E. Fetz, G. L. Bowlin, M. El-Newehy, X. Mo, Electrospinning nanofiber scaffolds for soft and hard tissue regeneration, J. Mater. Sci. Technol. 59 (2020) 243–261.

[28] M. Russo, G.K. Dirkx, C. Rosso, Patch augmentation in arthroscopic rotator cuff Surgery—Review of current evidence and newest trends, J. Clin. Med. 13 (17) (2024) 5066.

[29] Q. Wang, S. Zhou, L. Wang, R. You, S. Yan, Q. Zhang, M. Li, Bioactive silk fibroin scaffold with nanoarchitecture for wound healing, Compos. B Eng. 224 (2021) 109165.

[30] K. Panjapheree, S. Kamonmattayakul, J. Meesane, Biphasic scaffolds of silk fibroin film affixed to silk fibroin/chitosan sponge based on surgical design for cartilage defect in osteoarthritis, Mater. Des. 141 (2018) 323–332.

[31] J. Zhao, D. Zhang, Q. Lan, G. Zhong, Y. Liu, N. Holwell, X. Wang, J. Meng, J. Yao, B.G. Amsden, Y. Yu, F. Chen, Tendon decellularized matrix modified fibrous scaffolds with porous and crimped microstructure for tendon regeneration, ACS Appl. Bio Mater. 7 (2024) 4747–4759.

[32] C. Du, R. Wu, W. Yan, J. Fang, W. Dai, Y. Wang, J. Cheng, X. Hu, Y. Ao, X. Liang, Z. Liu, Ultrasound-controlled delivery of growth factor-loaded cerasomes combined with polycaprolactone scaffolds seeded with bone marrow mesenchymal stem cells for biomimetic tendon-to-bone interface engineering, ACS Appl. Mater. Interfaces 16 (2024) 292–304.

[33] E.G.J. Ripmeester, M.M.J. Caron, G.G.H. van den Akker, J. Steijns, D.A.M. Surtel, A. Cremers, L.C.W. Peeters, L.W. van Rhijn, T.J.M. Welting, BMP7 reduces the fibrocartilage chondrocyte phenotype, Sci. Rep. 11 (2021) 19663.

[34] Y. Zhu, B. Dai, S. Zhang, J. Liu, S. Xu, W. Liu, X. Chen, H. Zhang, Q. Li, F.O. Pang, W. Li, C. Wen, L. Qin, J. Xu, T. Ngai, Tissue mimetic membranes for healing augmentation of tendon-bone interface in rotator cuff repair, Adv. Mater. (2025) e2407358.

[35] S.H. Nile, Y.S. Keum, A.S. Nile, S.S. Jalde, R.V. Patel, Antioxidant, anti-inflammatory, and enzyme inhibitory activity of natural plant flavonoids and their synthesized derivatives, J. Biochem. Mol. Toxicol. 32 (2018) e22002.

[36] A.H. Faghfouri, M. Zarezadeh, O.M. Tavakoli-Rouzbehani, N. Radkhah, E. Faghfuri, H. Kord-Varkaneh, S.C. Tan, A. Ostadrahimi, The effects of n-acetylcysteine on inflammatory and oxidative stress biomarkers: a systematic review and meta-analysis of controlled clinical trials, Eur. J. Pharmacol. 884 (2020) 173368.

[37] J. Cegoñino, A. Calvo-Echenique, A. Pérez-del Palomar, Influence of different fusion techniques in lumbar spine over the adjacent segments: a 3D finite element study, J. Orthop. Res. 33 (2015) 993–1000.

[38] Issue Information, Arthritis Rheumatol. 69 (2017).

[39] I. Martínez-Vieyra, I. Hernández-Rojo, V.H. Rosales-García, A.E. Chávez-Piña, D. Cerecedo, Oxidative stress and cytoskeletal reorganization in hypertensive erythrocytes, Antioxidants 14 (2025) 5.

[40] J. Li, Jak-stat and bone metabolism, JAK-STAT 2 (2013) e23930.

[41] J. Chen, Q.-Y. Zhang, J. Tan, J. He, B.-Q. Qin, N. Sheng, H. Zhang, H.-Q. Xie, Enhanced fibrocartilage regeneration at the tendon-bone interface injury through

[42] extracellular matrix hydrogel laden with bFGF-overexpressing human urine-derived stem cells, Chem. Eng. J. 497 (2024) 154333.

[42] H.L. Moser, A.C. Abraham, K. Howell, D. Laudier, M.A. Zumstein, L.M. Galatz, A. H. Huang, Cell lineage tracing and functional assessment of supraspinatus tendon healing in an acute repair murine model, J. Orthop. Res. 39 (2021) 1789–1799.

[43] J.Y. Sunwoo, C.D. Eliasberg, C.B. Carballo, S.A. Rodeo, The role of the macrophage in tendinopathy and tendon healing, J. Orthop. Res. 38 (2020) 1666–1675.

[44] V. Arvind, A.H. Huang, Reparative and maladaptive inflammation in tendon healing, Front. Bioeng. Biotechnol. 9 (2021) 719047.

[45] A.G. Schwartz, F. Long, S. Thomopoulos, Enthesis fibrocartilage cells originate from a population of hedgehog-responsive cells modulated by the loading environment, Development 142 (2015) 196–206.

[46] K.L. Moffat, W.-H.S. Sun, P.E. Pena, N.O. Chahine, S.B. Doty, G.A. Ateshian, C. T. Hung, H.H. Lu, Characterization of the structure–function relationship at the ligament-to-bone interface, Proc. Natl. Acad. Sci. 105 (2008) 7947–7952.

[47] S. Thomopoulos, G.R. Williams, L.J. Soslowsky, Tendon to bone healing: differences in biomechanical, structural, and compositional properties due to a range of activity levels, J. Biomech. Eng. 125 (2003) 106–113.

[48] M. Abate, L. Di Carlo, G. Cocco, E. Sabatini, V. Salini, Estresse oxidativo e características ultrassonográficas do tendão anormal em jogadores de futebol de elite (um estudo piloto), Rev Bras Ortop (Sao Paulo) 56 (2021) 432–437.

[49] C. Zapp, A. Obarska-Kosinska, B. Rennekamp, M. Kurth, D.M. Hudson, D. Mercadante, U. Barayeu, T.P. Dick, V. Denysenkov, T. Prisner, M. Bennati, C. Daday, R. Kappl, F. Gräter, Mechanoradicals in tensed tendon collagen as a source of oxidative stress, Nat. Commun. 11 (2020) 2315.

[50] Y. Itoigawa, K. Yoshida, H. Nojiri, D. Morikawa, T. Kawasaki, T. Wada, A. Koga, Y. Maruyama, M. Ishijima, Association of recurrent tear after arthroscopic rotator cuff repair and superoxide-induced oxidative stress, Am. J. Sports Med. 49 (2021) 2048–2055.

[51] J. Cai, J. Xu, Z. Ye, L. Wang, T. Zheng, T. Zhang, Y. Li, J. Jiang, J. Zhao, Exosomes derived from kartogenin-preconditioned mesenchymal stem cells promote cartilage formation and collagen maturation for enthesis regeneration in a rat model of chronic rotator cuff tear, Am. J. Sports Med. 51 (2023) 1267–1276.

[52] Q. Liu, M. Chen, P. Gu, L. Tong, P. Wang, J. Zhu, Y. Xu, G. Lu, E. Luo, J. Liang, Y. Fan, X. Zhang, Y. Sun, Covalently grafted biomimetic matrix reconstructs the regenerative microenvironment of the porous gradient polycaprolactone scaffold to accelerate bone remodeling, Small 19 (2023) 2206960.

[53] Y. Li, C. Chen, J. Jiang, S. Liu, Z. Zhang, L. Xiao, R. Lian, L. Sun, W. Luo, M. Tim-yun Ong, M. Yuk-wai Lee, Y. Chen, Y. Yuan, J. Zhao, C. Liu, Y. Li, Bioactive film-guided soft–hard interface design technology for multi-tissue integrative regeneration, Adv. Sci. 9 (2022) 2105945.

[54] D.F.E. Ker, D. Wang, A.W. Behn, E.T.H. Wang, X. Zhang, B.Y. Zhou, Á.E. Mercado-Pagán, S. Kim, J. Kleimeyer, B. Gharaibeh, Y. Shanjani, D. Nelson, M. Safran, E. Cheung, P. Campbell, Y.P. Yang, Functionally graded, bone- and tendon-like polyurethane for rotator cuff repair, Adv. Funct. Mater. 28 (2018) 1707107.

[55] X. Xie, J. Cai, Y. Yao, Y. Chen, A.u.R. Khan, J. Wu, X. Mo, A woven scaffold with continuous mineral gradients for tendon-to-bone tissue engineering, Compos. B Eng. 212 (2021) 108679.

[56] X. Xie, J. Cai, D. Li, Y. Chen, C. Wang, G. Hou, T. Steinberg, B. Rolauffs, M. El-Newehy, H. El-Hamshary, J. Jiang, X. Mo, J. Zhao, J. Wu, Multiphasic bone-ligament-bone integrated scaffold enhances ligamentization and graft-bone integration after anterior cruciate ligament reconstruction, Bioact. Mater. 31 (2024) 178–191.

[57] L. Du, J. Wu, Y. Han, C. Wu, Immunomodulatory multicellular scaffolds for tendon-to-bone regeneration, Sci. Adv. 10 (2024) eadk6610.

[58] E.R. Sanpaolo, C. Rotondo, D. Cici, A. Corrado, F.P. Cantatore, Jak/Stat pathway and molecular mechanism in bone remodeling, Mol. Biol. Rep. 47 (2020) 9087–9096.

[59] C. Zhao, X. Wang, L. Gao, L. Jing, Q. Zhou, J. Chang, The role of the micro-pattern and nano-topography of hydroxyapatite bioceramics on stimulating osteogenic differentiation of mesenchymal stem cells, Acta Biomater. 73 (2018) 509–521.

[60] S. Suvarnapathaki, X. Wu, D. Lantigua, M.A. Nguyen, G. Camci-Unal, Hydroxyapatite-incorporated composite gels improve mechanical properties and bioactivity of bone scaffolds, Macromol. Biosci. 20 (2020) e2000176.

[61] C.V. Maduka, A.D. Schmitter-Sánchez, A.V. Makela, E. Ural, K.B. Stivers, H. Pope, M.M. Kuhnert, O.M. Habeeb, A. Tundo, M. Alhaj, A. Kiselev, S. Chen, A. Donneys, W.P. Winton, J. Stauff, P.J.H. Scott, A.J. Olive, K.D. Hankenson, R. Narayan, S. Park, J.H. Elisseeff, C.H. Contag, Immunometabolic cues recompose and reprogram the microenvironment around implanted biomaterials, Nat. Biomed. Eng. 8 (2024) 1308–1321.